SiO_2 Trench Embedded Field Effect Transitor for Bio-sensing Applications

A
Thesis Submitted
in Partial Fulfilment of the Requirements
for the Degree of

DOCTORATE OF PHILOSOPHY

By

MONICA NAOREM

Centre for Nanotechnology
Indian Institute of Technology Guwahati

January, 2022

DECLARATION

This is to certify that the thesis entitled "**SiO_2 Trench Embedded Field Effect Transitor for Bio-sensing Applications**", submitted by me to the *Centre for Nanotechnology, Indian Institute of Technology Guwahati* for the award of the degree Doctor of Philosophy. This is an oroginal research work carried out by me under the supervision of **Prof. Roy P. Paily**. The contents of the thesis, in full or in parts, have not been submitted to any other Institute or University for the award of any degree or diploma.

Monica Naorem
Registration No. 166153101
Centre for Nanotechnology
Indian Institute of Technology Guwahati
Guwahati-781039, Assam, India

CERTIFICATE

It is certified that the work contained in the thesis entitled "**SiO_2 Trench Embedded Field Effect Transitor for Bio-sensing Applications**"by **Monica Naorem** (166153101), a research scholar in the *Centre for Nanotechnology, Indian Institute of Technology Guwahati* for the award of the degree of Doctor of Philosophy, is a record of an original research work carried out by her under my supervision and guidance. This thesis has fulfilled all requirements as per the regualations of the institute, and in my opinion has reached the standard needed for submission. The results embodied in this thesis have not been submitted to any other Unversity or Institute for the award of any degree or diploma.

Date:

Prof. Roy P. Paily

Centre for Nanotechnology & Department of Electronics and Electrical Engineering

Indian Institute of Technology Guwahati

Guwahati-781039, Assam, India

ACKNOWLEDGEMENT

I would like to convey my sincere gratitude to my supervisor, Prof. Roy P. Paily for giving me this wonderful opportunity to carry out my research work under his guidance. I am highly obliged to him for his support, encouragement, and for providing the facilities required for accomplishment of the research objectives. Without his constant support, I would not have come this far.

I extend my thanks to my doctoral committee members, Prof. Siddhartha Sankar Ghosh (Chairman) for helpful suggestions, discussions, adding important insights to my experimental work and co-authoring my research papers. Dr. Arun Tej Mallajosyula and Dr. Partho Sarathi Gooh Pattader for continuously evaluating my thesis work and for giving valuable ideas and suggestions for improvement. I would like to thank Center for Nanotechnology and Centre for Excellence in Nanoelectronics & Theranostic Devices (CENTD) for providing me with the much needed instrument facilities to carry out all my experiments. I thank Electronics and Electrical Engineering Department for allowing to access lab facilities to complete my reasearch work. My special thanks goes to Mrs. S. Josephine, Technical Officer, who has helped us to utilize the lab resources efficiently.

I sincerely thank my seniors Dr. Jitendra Kumar, Dr. Shyam Trivedi, Dr. Ujjwol Barman, Dr. Namami Goswami, Siddhanta Roy, Thomash, Pralay, Satyajit. Also I would like to thank my mates Birjit, Raveesh Ji, Paromita, Himakshi, and Atanu for being a part of the wonderful memories made in the time spent in the lab. My sincere thanks goes to Siddhanta Roy and kasturi Gogoi from CNT, who have helped me in numerous ways in the form of fruitful technical and friendly discussions.

I would like to thank my collaborators: Rajan Singh, Sampriti Ghosh, and

Plaboni Sen, who were not only good researchers, but also good colleagues. I would like to extend my deepest gratitude towards my Da Somorjit, and Da Franco for being such great companions during my tenure at IIT Guwahati. They always treated me like their younger sister and were with me whenever I needed them.

I would like to specially mention Lenin Laitonjam for his constant support, encouragement and care. My special thanks also goes to my friends to Aruna, Debeni, Menan, Sophia, Shweta, and Neelam, without them my life at IIT Guwahati would not have been memorable.

Last but not the least, I extend my heartfelt thanks to my parents for their selfless love, encouragement, and support in my journey of life. I thank them for giving me the best possible education which has helped me in achieving whatever I have today. They were the ones who inspired me to sow the seeds of hard work, sincerity and dedication in my life. I thank my elder brother Atyaraj for guiding me in all matters since childhood, and showing the right way with love and encouragement. I thank my younger brother Biki for giving me encouragement, love and care. Also I thank my sis-in-law Indira for her support. I owe everything whatever I have earned in these years to my family. I thank the Almighty for gifting me with such wonderful people.

ABSTRACT

Biologically sensitive field-effect transistors (Bio-FETs) couple a transistor device with a bio-sensitive layer that can specifically detect biomolecules. There are many challenges involved in developing a Bio-FET such as selecting a suitable device's channel structure and channel material, provision of a sensing film layer on the active site of field-effect transistor (FET), setting up a receptor on the sensing film layer to enable ion detection, the inclusion of liquid holding facility, etc. Moreover, rapid response and higher sensitivity are necessary. This thesis proposes a structure that has a SiO_2 trench along with a reservoir that removes the need for any extra mold for containing the analyte liquid. The inbuilt trench structure brings additional benefits such as ease in the analyte pouring during the sensing, helps in the storage of liquid, minimizes the overflow of the analyte liquid and improves gate control by an increment in effective oxide capacitance.

Four contributions have been made in this thesis. As the first contribution, a SiO_2 trench integrated FET is designed and characterized for biosensing applications. The device was fabricated using photolithography followed by etching steps. The fabricated trench surface is characterized using Atomic force microscopy (AFM), and contact angle analysis. Basic trench embedded FET device was electrically characterized with KCl as an ionic liquid channel. FET structure modeling was also carried out to estimate the effective Cox for the trench SiO_2 structure. It is observed that the total capacitance after the inclusion of Debye length is $1.29 \times 10^{-4} F/m^2$. Further, the number of ions is also calculated from the electrical characteristics, and it is almost comparable with the number of ions in the molar solution. Overall, the proposed fabricated structure, although simple, enables to accommodate any liquid as a channel and provides an easy way to

develop electrolyte-based sensors.

The second contribution of the thesis is the fabrication of high-performance hydrogen peroxide (H_2O_2) sensing field-effect transistor (FET) using reduced graphene oxide - polypyrrole (rGO/PPy) nanocomposite. The fabricated SiO_2 trench structure was used not only for holding H_2O_2 but also for sensing purpose. The morphology and structure of the rGO/PPy nanocomposite were analyzed and confirmed their bonding. The output electrical signal changes as the concentration of H_2O_2 increases. The device shows a fast response of 5 s and is highly stable with excellent sensitivity. The detection limit obtained is 10 pM at the appropriate signal-to-noise ratio (S/N) of the sensing electrical signal. The device is highly selective towards H_2O_2. The device structure may be employed for other liquid sensing applications.

The third contribution of the thesis demonstrates the application of graphene oxide-silver (GO/Ag) nanocomposite to develop a non-enzymatic high-performance glucose-sensing field-effect transistor (FET). Lithography and etching processes are used to fabricate the SiO_2 trench embedded FET. The bonding of the GO/Ag nanocomposite was validated by analysing their shape and structure. As the concentration of glucose rises (1 μM to 10 mM range), the output electrical signal changes. With a 1 μM limit of detection (Signal to Noise ratio, S/N $>$ 3), the sensor has a fast response time of fewer than 5 seconds. It also demonstrated great long-term stability, outstanding reproducibility, and excellent glucose selectivity. This sensor has notable characteristics such as ease of production, simplicity of usage, and small size. It has the potential to fabricate portable glucose sensors for point-of-care sensing in the future. Additional liquid sensing applications could benefit from the fabricated sensor structure.

The fourth contribution of the thesis is the development of Lactate dehydro-

genase (LDH) electrochemical detection method in SiO_2 trench embedded device. Lactate functionalised GO/Ag nanocomposite was used to conduct the enzymatic reaction in channel. The device's current changes in real-time when the conjugation reaction between LDH and Nicotinamide adenine dinucleotide (NAD^+) occurs in the presence of Lactate on the device's channel, verifying the detection of Lactate dehydrogenase (LDH). According to research, the buildup and generation of ROS appear to contribute to the conversion of normal cells to cancer cells by mediating genomic instability, oncogenic growth, extracellular matrix (ECM) independency, and enhanced motility. The device was also investigated with an LDH generated from the MDA-MB-231 breast cancer cell line. The device was shown to be capable of detecting raised LDH levels in malignant cells, which is the initial step in diagnosing various kinds of acute cancer sickness. The device may be enhanced further to fulfil the demands of a marketable product while keeping the core functioning principle the same.

Contents

List of Figures

List of Tables

Chapter 1

INTRODUCTION

1.1 Background

A biosensor is a device that generates signals according to the concentration of an analyte in a biological or chemical reaction to monitor it [1]. The invention of enzyme electrodes by Leland C. Clark in 1962 marked the beginning of the biosensor era. Since then, researchers from a variety of domains, including VLSI, physics, chemistry, and material science, have collaborated to produce more sophisticated, dependable, and robust biosensing systems. These devices have applications in medicine, disease monitoring, drug discovery, detection of contaminants, agriculture, biotechnology, military applications, and biowarfare detection and prevention [2, 3]. Generally, biosensors are made up of two parts: a biological recognition element and a sensor element. As functional hybrid systems, they advantage from the coupling of the unique recognition and signal-amplification properties of biological systems. As a result, combining biologically active materials with various types of transducers allows for the development of highly sensitive, specific, selective, and dependable biosensors. Based on the biological recognition element, there are

various types of biosensors such as DNA biosensors, Enzyme-based, tissue-based, Cell-based, immunosensors, and so on. DNA biosensors are generally made up of an immobilised DNA strand that uses DNA–DNA hybridization to detect the complementary sequence [4]. On other hand, an enzymatic biosensor is made up of an enzyme that detects and interacts with the target analyte to generate a chemical signal [5]. Plant and animal tissues are used to make tissue-based sensors. Although the stability of tissue-based sensors is acceptable, the detection time is long and the specificity is also low [6]. Cell-based sensors are exploited in the detection of cells metabolism and the analysis interaction of drugs and cells. Immunosensors are based on the fact that antibodies have a high affinity for their antigens, meaning they precisely attach to infections or poisons, or interact with immune system components in the host [2].

On the other hand, based on the transducing mechanism of a sensor, the biosensors can be of many types such as piezoelectric biosensors, thermal-detection biosensors, optical detection biosensors, electrochemical biosensors, etc. The quartz crystal microbalance and the surface acoustic wave device are two forms of piezoelectric biosensors. They are based on the detection of changes in a piezoelectric crystal's resonant frequency as a result of mass changes in the crystal structure [2]. Thermal biosensors monitor the heat energy emitted or absorbed during oxidation. These types of sensors can calculate the number of oxygen equivalents used by strong oxidation agents during the oxidation of organic contaminants. Optical biosensors work by detecting optical signals generated by biological recognition of the sample, either through biocatalytic or bioaffinitive processes [7]. The electrochemical biosensor is a common sensing device that works by converting biological processes into electrical signals. It can be categorized as conductimetric, amperometric, or potentiometric depending on the parameter analyzed.

Field-effect transistor (FET) based biosensors stand out among the many types of established electrochemical biosensing technologies because of thier amplification ability. They are also a suitable choice for applications demanding high sensitivity and quick reaction times [8].

1.2 Bio-FET

In recent years, biosensors based on field effect transistors (FETs) have been successfully used to diagnose a variety of acute disorders. Since its first realisation in 1980 by Caras and Janata, field-effect transistor (FET)-based biosensors (BioFETs) have made significant development, particularly in the recent decade. BioFETs have recently emerged as one of the most important branches of biosensors. Indeed, almost half-century since Bergveld's 1970 development of the first ion-sensitive field-effect transistor (ISFET), we have seen these transducers evolve in a variety of biosensor applications [9]. The working mechanism of a FET biosensor distinguishes it from other types of device-based electrochemical biosensors. Due to their ability to immediately translate the interaction with analytes taking place on the FET surface into a readable signal, FET is a good choice for the designated sensors. As a result, the analytes do not need to be marked, and we refer to this technology as a label-free biosensor technique. FET-based biosensors are a three-electrode system in terms of electrochemistry, with the source, drain, and gate electrodes. The change of the resistance between source and drain electrodes is caused by the accumulation and modification of charged analytes at the solution interface. The amplitude of the modulation can be increased and quantified by adjusting the channel's resistance through a third electrode (gate) [10]. Due to their advantage of miniaturisation, Bio-FETs have a great potential to become

one of the best sensing technologies for point-of-care (PoC) medical applications in today's era, where there is always a demand for portable label-free diagnosis [11, 12, 13, 14]. For particular interactions with biomolecules, such as enzymatic reactions, DNA hybridization, and antibody–antigen reactions, a variety of FET-based biosensors can be used. Depending upon the interactions, BioFET can classified into three categories: enzyme-based FETs (ENFETs), cell-based FETs, and immunodetection-based FETs. ENFETs, which integrate ion-sensitive field-effect transistors (ISFETs) and enzymes, are dependent on biocatalytic reactions that modify the charge at the gate surface and produce an electrical signal that is proportional to the concentration of enzyme substrate. Various enzymes, such as glucose oxidase, urease, horseradish peroxidase, and others, are researched in the ENFETs [15, 16, 17]. Cell based FETs are used in the detection of cellular metabolism and the investigation of drug-cell interactions. Inside cells, FETs can also record electric potentials. A new approach has been reported by a group of researchers in which a SiO_2 nanotube is synthetically built on top of a nanoscale FET [18]. The nanotube can pass through the cell membrane and deliver the cytosol into the interaction with the FET, allowing it to collect the intracellular transmembrane potential. Subsequently, the most often adopted biosensors are immunoFETs. By detecting charged antigens relevant to critical diseases employing immobilised antibody modified FETs, it is expected to provide rapid and important information on the very first therapy. ImmunoFET biosensing devices for medical applications, on the other hand, have not yet been fully implemented due to two limitations. The first possible major challenge is that without pretreatment, ImmunoFET sensors have trouble identifying macromolecules in physiological solutions. The second is to get around the Debye length's inherent filtering [19]. As a result, adjusting the Debye length based on the height of the adsorbed recep-

tor is crucial for increasing the sensitivity of FET detection. Over the years, the liquid-based FET has been extensively used for the applications like bio-molecule detection, analyte based biosensor, pH sensing, etc[20, 21, 22, 23, 24, 25].

1.2.1 Applications

Considering various types of Bio-FETs, we look into the applications of H_2O_2, glucose, and Lactate dehydrogenase (LDH) sensing in our fabricated device. The reasons for choosing these specific analytes for sensing are listed below.

Hydrogen peroxide (H_2O_2)

Analyte such as H_2O_2 is a vital component in the human body since it aids in the signalling of healthy cell pathways and is also essential for other cell functions such as immune system function, cell proliferation, and so on [26, 27]. And it is one of the reactive oxygen species (ROS) linked to a variety of diseases, including atherosclerosis, cancer, and Alzheimer's disease [28, 29, 30]. Also, it is a byproduct of metabolism that can cause a variety of problems such as disintegrating into hydroxyl radicals, which attack biochemicals like proteins and DNA. Additionally, high levels of H_2O_2 can damage skin, injure human organs and the central nervous system, and even cause cancer, which classifies it as a carcinogen, according to the World Health Organization [31]. As a result, an easy approach to consistently and accurately detect H_2O_2 is required for clinical diagnostics and patient monitoring.

Glucose

Subsequently, glucose is also an essential component of the primary health system and a vital source of energy in the human body, providing the energy needed for daily duties and activities [32]. On the other side, excessive glucose consumption

in the body causes weight gain and health problems. Diabetes mellitus and its consequences are caused by high blood glucose levels in the body [33]. The fact that a rising number of young people have diabetes is cause for alarm [34]. By 2025, the number of individuals affected by this serious global public health hazard, which can impair nerves, blood vessels, and organs, is predicted to double to 300 million [35]. Continuous blood glucose monitoring (CGM) can lower the risk of hypoglycemia or hyperglycemia-related consequences, allowing diabetes to be effectively managed and controlled [36]. Cancer cells typically multiply quickly, consuming a lot of energy in the process of growing. This necessitates a large amount of glucose. Hypoxic cancer cells consume glucose for glycolysis and generate lactate, which oxygenated cancer cells use [37]. If cancer cells require a lot of glucose, eliminating sugar from our diet must help prevent cancer from spreading and possibly even prevent it from starting in the first place. Unfortunately, it is not simple as that because all of our healthy cells require glucose, and there is no way to command our systems to provide glucose to healthy cells while denying it to cancer cells. As a result, for clinical diagnostics and patient monitoring, an easy technique to consistently and correctly measure glucose is necessary.

Lactate dehydrogenase (LDH) enzyme

Cancer is a generic term that represents a large group of diseases that can affect any part of the body. The most promising aspect of obliterating such a plethora of diseases is its early detection and accurate diagnosis. One such method of diagnosing is the presence of biomarkers, which are produced in response to various disorders. Recently, biosensor-based point-of-care (POC) diagnostic devices hold utmost importance in the detection of several diseases, especially cancer. However, the presence of numerous cancer specific biomarkers makes the development of

biosensors more challenging [38, 39, 40, 41, 42, 43, 44]. As per the reports of the National cancer registry program, breast cancer (BC) is one of the most common cancers among urban women in India; with an annual surge of approximately 2%, in comparison to the other cancer. The projected number of breast cancer cases in 2020 was 10% of all cancer and the mortality rate of breast cancer is also two-fold higher than the death/mortality rate in western countries [41].

One of the prominent hallmarks of cancer is the increased energy requirements, which is accounted for by the higher cellular proliferative activity of the malignant cells. Metabolic changes in malignant cells are associated with increased anaerobic glycolysis, which ultimately results in the production of a large amount of lactic acid (Warburg effect). Thus, the LDH level is found to be commonly increased in cancer patients, which results in poor clinical outcome and resistance to therapy. Thus, the determination of LDH is of utmost importance in the diagnosis of cancer.

As a result of the above-mentioned issues, a portable and easy diagnostic technology with miniaturisation possibilities, such as microfluidics-based cellular diagnostics, is needed. In addition, the sensing area's design must be efficiently produced.

1.3 Challenges

1.3.1 FET's channel architecture

Various types of liquid-based FETs have been discussed depending on the channel architecture and, the method of applying the gate voltage [45, 46, 47, 48, 49, 50]. In a liquid-based FET, a major challenge would be the practical realization of a liquid storage such that it would also act as the channel. Previous approaches for the fabrication of liquid channel FET to hold liquid includes intricate design

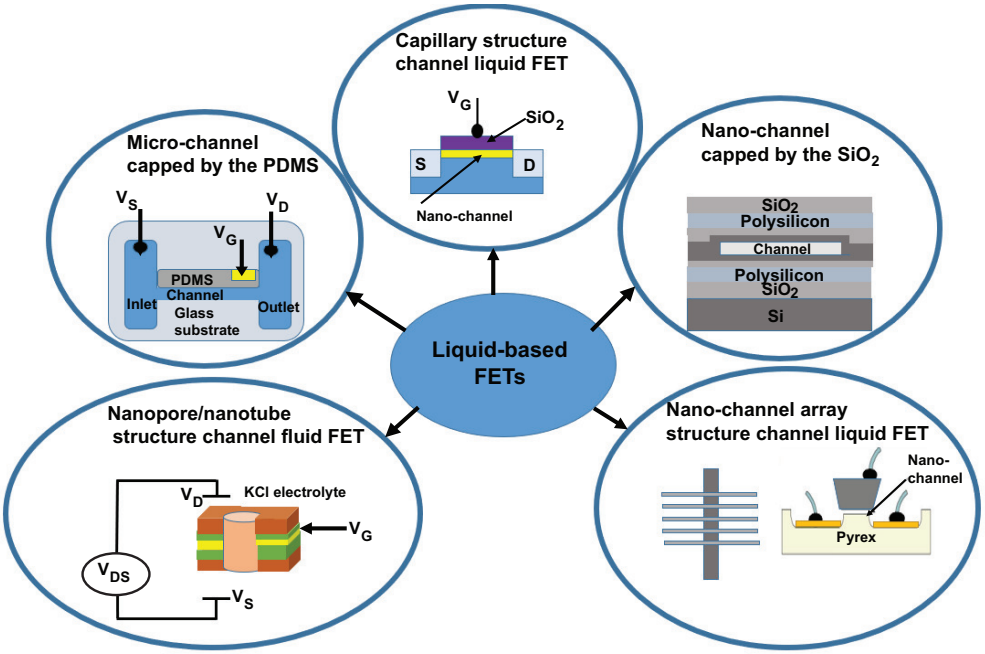

Figure 1.1: Different structures of liquid-based FETs

with capping, capillary, etc. [45, 46, 47, 48, 49, 50]. Some of these liquid channel FET structures are summarised in Figure. 1.1. In one case, a nano-channel chamber is formed by capping with gate oxide [49, 51]. They employed standard photolithography and wet etching to fabricate nano-channels, and liquid reservoirs on the pyrex wafer. The capping is achieved with a dry oxidized silicon gate [49]. Another group used Polydimethylsiloxane (PDMS) layer for capping to seal the nano-fluidic device. They also fabricated their nano-channel FET using photolithography, wet etching, and oxygen plasma bonding techniques [52]. The channel can be made of nanopore/nanotube structures using the Porous alumina membrane or Focused ion beam (FIB) techniques [53, 54]. Sputtering and barrier-type anodization processes are also involved in the fabrication of a few channel structures. Several nanotubes are required to realize a single device. These designs are used for drug delivery, desalination, DNA sequencing, and energy conversion [53]. In summary, all these structures demand multiple steps of fabrication. The

current in the micro/nano-channels is modulated by the gate voltage [50]. Therefore, these designs need either a reference electrode or a top gate adjacent to the liquid channel to characterize the device's electrical performance, and this would also involve additional fabrication steps. Hence, the device structure includes a SiO_2 trench and a reservoir that could eliminate the requirement for an additional mould to hold the analyte liquid.

1.3.2 Channel material for FET

Another most challenging feature of using FET to detect a specific analyte is choosing a channel material. Carbon nanoparticles and metal-based nanomaterials are the two primary kinds of nanomaterials. Graphene, graphene oxide, carbon nanotubes, carbon nanofibers, nanodiamond, and fullerene are the most prevalent carbon nanomaterials. Because of its excellent conductivity, large surface area, and carrier mobility, reduced graphene oxide (rGO) is a promising channel material [55, 56, 57, 58]. It also has a high density of receptor sites, which allows it to detect a wide range of analytes with great sensitivity [57, 59, 60]. Conducting polymers, such as polypyrrole (PPy), polyaniline, and their variants, have better sensing properties and display rapid reaction and recovery [61, 62, 63, 64, 65]. Because of its redox capabilities, reasonable chemical stability against ambient conditions, strong electrical conductivity, and surface charge controllable features, polypyrrole (PPy) is a popular conducting polymer [66, 67, 68, 69]. As a result, we investigate the benefits of rGO and PPy and select their nanohybrids for improved overall sensing performance for H_2O_2 detection [10]. Futhermore, among the many metal-based nanomaterials used in biomedical applications, silver nanoparticles (AgNPs) are one of the most important and fascinating nanomaterials. Nanoparticles, particularly AgNPs, play an essential role in nanoscience and

nanotechnology, especially in nanomedicine. We chose their nanohybrids with GO for increased overall sensing performance due to their biomolecule binding property. Moreover, the capabilities of metal nanoparticles can be improved by stabilising them with a suitable substance. GO provides a chemically and physically stable surface for metal nanoparticles [70, 71, 72]. Charge transfer has also been observed between GO and other metals and semiconductor nanoparticles. Metal nanoparticles and GO have a synergistic property that makes electrocatalysis a viable alternative [73]. Therefore, we investigate the benefits of GO and Ag NPs, as well as their nanohybrids, to improve overall sensing performance over the previously reported glucose sensor. Finally, the Ag NPs have the ability to bond with lactate, which is important for LDH sensing. As a result, lactate functionalized GO/Ag nanocomposite was chosen to conduct LDH assays and to detect LDH on the device.

1.4 Motivation

The depth of the well and the amount of liquid are interrelated but designing or patterning of the depth on the substrate is difficult, this leads to more research on this field. The volume of liquid could be increased by increasing the channel length, but the device's resistance will increase, reducing the transconductance. On the other hand, increasing the depth of the trench may improve device performance, but it may also result in leakage current. Further, it is also essential to the detect target of interest at low concentrations using the proper materials for the bio-recognition component. The above observations motivated the importance of FET structure and dimension in biosensors.

The theoretical and practical aspects of the approach that would be required

to develop it into a reliable and repeatable technology have been studied in this work, which recognises the FET with SiO_2 trench structure for a liquid storing and sensing biomolecules.

1.5 Problem Definition

It was indicated in the earlier discussions that embedding a trench could be a viable option for liquid holding and biomolecule sensing. Some of the advantages of using trench structure include reducing analyte liquid overflow, which is a major cause of electrode deterioration and sensor breakdown, and trench structure increases effective oxide capacitance, which aids in gate control; and relatively fast speed, which is probably the most effective feature for the quality sensor. As a result, research efforts have been made to optimise and analyse with an ionic liquid channel in order to fabricate SiO_2 trench embedded FETs. And the results obtained from these investigations have been applied to the fabrication of rGO/PPy nanocomposite FETs and GO/Ag nanocomposite FETs for bio-sensing applications. The main objectives of the thesis can be listed as follows:

1. Fabrication of an ionic liquid channel FET for biosensing application.

2. Detection of Hydrogen Peroxide Using rGO/PPy Nanocomposites in Silicon Dioxide Trench Embedded Field Effect Transistor.

3. Non-enzymatic glucose detection using GO/Ag nanocomposite in Silicon Dioxide Trench Embedded Field Effect Transistor.

4. Lactate functionalised GO/Ag nanocomposite FET for label free lactate dehydrogenase detection.

1.6 Thesis Outline

The thesis has been organized into six chapters. The contents of each chapter can be briefly outlined as follows.

Chapter 1 generalised introduction chapter which details the fundamental aspects of biosencors and their types, various channel architecture along with motivation and organisation of the thesis work.

Chapter 2 describes the fabrication steps process of the device using lithography and etching techniques, and electrical characterization with KCl as the ionic liquid channel. This chapter explores the characterization of etched surface of the SiO_2 trench. Furthermore, this chapter analyses the number of ions from the electrical characterization and compared with the number of ions in molar solutions.

Chapter 3 describes the the high-performance hydrogen peroxide (H_2O_2) sensing field-effect transistor (FET) using reduced graphene oxide - polypyrrole (rGO/PPy) nanocomposites. The morphology and structure of the rGO/PPy nanocomposites were analyzed and confirmed their bonding using different characterizing intruments. For the sensing performance analysis, different concentrations of H_2O_2 have been tested. With an appropriate signal-to-noise ratio (S/N) of the sensing electrical signal, the detection limit of H_2O_2 in our fabricated device is 10 pM. The fabricated device shows a low response time of 5 s and highly selective towards H_2O_2.

Chapter 4 describes demonstrates the application of graphene oxide-silver (GO/Ag) nanocomposite to develop a non-enzymatic high-performance glucose-sensing field-effect transistor (FET). The bonding of the GO/Ag nanocomposite was validated by analysing their shape and structure using different instruments.

The sensing analysis was performed using 2450 source meter and power supply. The output current changes as the concentration of glucose increase. The detection limit obtained was 1 μM limit of detection (Signal to Noise ratio, S/N > 3). With a response time of less than 5 seconds, the sensor is extremely fast. It also showed high glucose selectivity, excellent long-term stability, and excellent repeatability. This sensor stands out for its ease of manufacture, simplicity of use, and small size.

Chapter 5 describes the designing of a SiO_2 trench embedded nanoconjugate channel FET based biosensor, which can be used to detect lactate dehydrogenase (LDH) enzyme as well as the cell line secreted LDH enzyme. In this chapter, when the conjugation reaction between LDH and NAD^+ occurs in the presence of Lactate on the device's channel, the device's current changes in real-time, confirming the detection of LDH. The optimum temperature for the LDH enzymatic reaction was determined using a temperature dependence analysis. This work probably is the first to report an LDH detection FET based on the occurrence of a chemical reaction in real time using its output characteristics.

Chapter 6 presents conclusive remarks for this work and a brief discussion on future scopes of this work.

Chapter 2

FABRICATION OF IONIC LIQUID CHANNEL FIELD EFFECT TRANSISTOR

2.1 Introduction

In this chapter, a simple back gating design with the ionic liquid channel inside the trench of SiO_2 is introduced. The proposed design modified the dielectric layer (SiO_2) as a liquid chamber, and while doing this we could achieve higher gate capacitance and hence better gate control. The proposed design simplifies the liquid channel realization. Moreover, in proposed device, one type of carrier (cation or anion) can enginner for wholly responsible for the current conduction by simply applying a suitable gate voltage. The trench is fabricated by following a standard photolithography process with the help of selective etching of Aluminium and SiO_2 using Aluminium etchant solution and Buffered oxide etch (BOE) solution, respectively. The SiO_2 etched surface's roughness and hydrophobicity are characterized using AFM and contact angle analysis, respectively, to study the

effect of the selective etching, and chamber's liquid holding capabilities. The effective oxide capacitance ($C_{ox_{eff}}$) by approximating the shape of the etched SiO_2, it is found as 20% more than a uniformly thick 300 nm SiO_2. This increase in capacitance enhances the transconductance of the device. The numbers of K^+ and Cl^- in molar solution is also approximately similar to the numbers calculated from the current-voltage curve. In summary, this chapter demonstrates a novel structure of an ionic liquid channel FET that provides three advantages (1) enhanced capacitance and transconductance, thereby increased sensitivity of the device, (2) a CMOS compatible simple container for incorporating the analyte, (3) can engineer single polarity ions to govern the current flow with a back gate control.

2.2 Materials

Buffer oxide etch (BOE), 2-propanol, Acetone, Sulfuric acid (H_2SO_4), Nitrous acid (HNO_3) Hydrogen peroxide (H_2O_2), and N-methyl pyrrolidone (NMP) were procured from Sigma Aldrich, India. Potassium chloride (KCl) of 99 % purity from HIMEDIA was procured. The De-ionised (DI) water was used in all the experiments. Phosphorous doped of $< 100 >$ oriented Si wafers of 500 μm thick were purchased from University Wafer.

2.3 Fabrication Process

Figure 2.1 describes the fabrication process flow. The device was fabricated on n-type $< 100 >$ oriented silicon wafers with a thermally grown SiO_2 of 300 nm thickness. First of all, the substrate is cleaned using Piranha solution of [3:1]

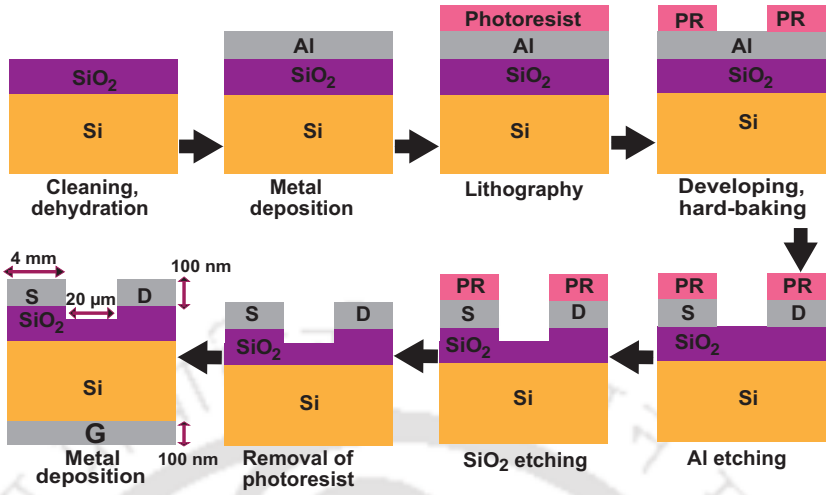

Figure 2.1: Steps of the device fabrication

ratio of concentrated H_2SO_4 and H_2O_2, and then treated with ozone for removal of hydrocarbon contamination [74]. Next, Aluminium (Al) was deposited using thermal deposition for making the source and the drain electrodes. The thickness of deposited Al was 100 nm. Using conventional UV lithography technique with positive photoresist S1813, a 20 μm channel length is patterned on the substrate under a direct laser writing instrument (Dilase 250). The laser exposed portion was open with the help of the developer solution. Next, we proceed for aluminium etching using aluminium etchant solution which is made of $H_3PO_4 : HNO_3 : H_2O$ = [19:1:4] ratio [75]. The sample is cleaned with DI water 4-5 times after Al etching and kept for heating at 120∘C for 15 minutes. The patterned contacts have a dimension of 2 mm $\times$ 4 mm.

For SiO_2 etching, we tried Hydrofluoric acid (HF) with different percentages. Etching was violent and oxide was getting damaged, therfore we used Buffer oxide etch (BOE), which is the composition of ammonium fluoride (NH_4F) and hydrofluoric acid (HF) [10:1]. The ammonium fluoride (NH_4F) is added to minimize the photoresist attack and maintain HF concentration. In this step of SiO_2 etching, we

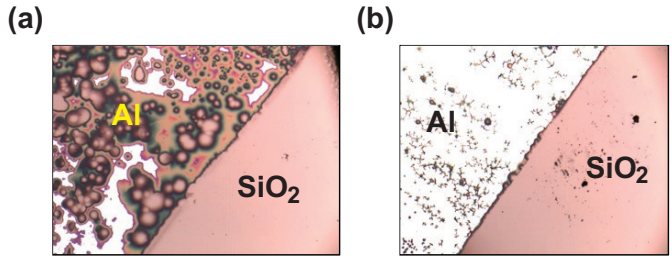

Figure 2.2: Optical image of Aluminium (Al) and SiO_2 etched surface (a) BOE etched, (b) BOE + Glycerin [5:2]

added some amount of glycerin to the BOE solution to protect the metal portion from HF [76]. As shown in Figure 2.2, the [5:2] ratio of BOE + glycerin helps in the protection of the Al layer from acid attack.

Finally, using a PG remover solution (NMP), the photoresist is removed. Then for bottom contact, Al metal was deposited on the bottom side of the substrate using thermal evaporation. The dimensions of the fabricated device are summarized in Table 2.1. This device has the advantage of having a trench inside SiO_2 which can store liquid.

Table 2.1: Fabricated device parameters

Parameter	Channel length	Channel width	Oxide Trench Depth	Contact thickness	Contact dimension
Value	20 um	2 mm	100 nm	100 nm	2×4 mm

2.4 Results and Discussions

2.4.1 SiO_2 etched surface analysis

The contact angle analysis was carried out using a Goniometer (Model No. HO IAD-CAM-01B) to quantify the hydrophilic nature of SiO_2 etched surface. Figure

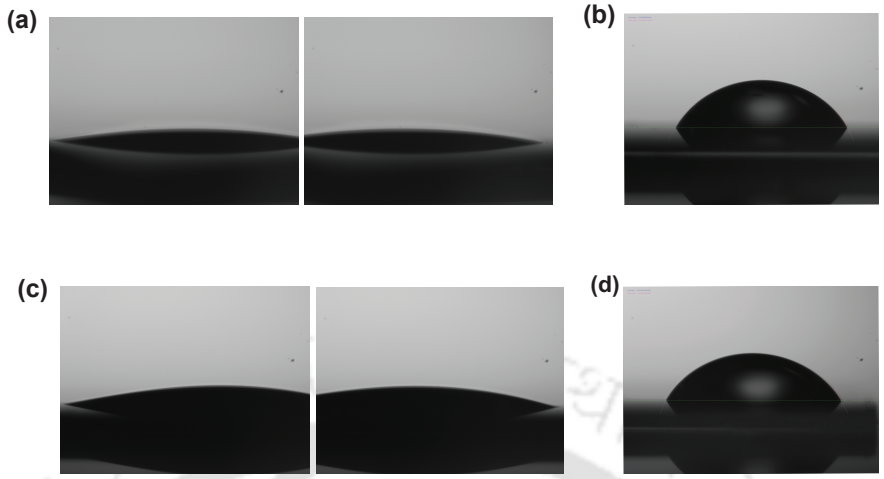

Figure 2.3: (a) Contact angle measurement for DI water over BOE etched surface, (b) Contact angle measurement for DI water over BOE + Glycerine etched surface, (c) Contact angle measurement for 0.01 mM KCL over BOE etched SiO_2 surface, (d) Contact angle measurement for 0.01 mM KCL over BOE + Glycerine etched surface

2.3 shows the contact angle over SiO_2 surface etched by BOE, and BOE with glycerine composition, and details are shown in Table 2.2. For a reference standard, DI water was used. The contact angle increases as the surface is etched with the BOE and glycerine composition. To quantify the results of the adhesion properties of the liquid on an etched SiO_2 surface, contact angle measurements are

Table 2.2: Contact angle analysis of etched surface SiO_2

Sample	**DI Water**		**0.01 mM KCl**	
Substrate	BOE etched surface	BOE + glycerin etched surface	*BOE* etched surface	BOE + glycerin etched surface
Left contact angle	1.5°	61.2°	10.8°	69.62°
Right contact angle	17.8°	65.49°	12.3°	63.43°
Average contact angle	9.65°	63.34°	11.5°	66.52°
Hydrophilic	**High**	**Moderate**	**High**	**Moderate**

performed. The average contact angle for the 0.01 mM of KCl solution is found

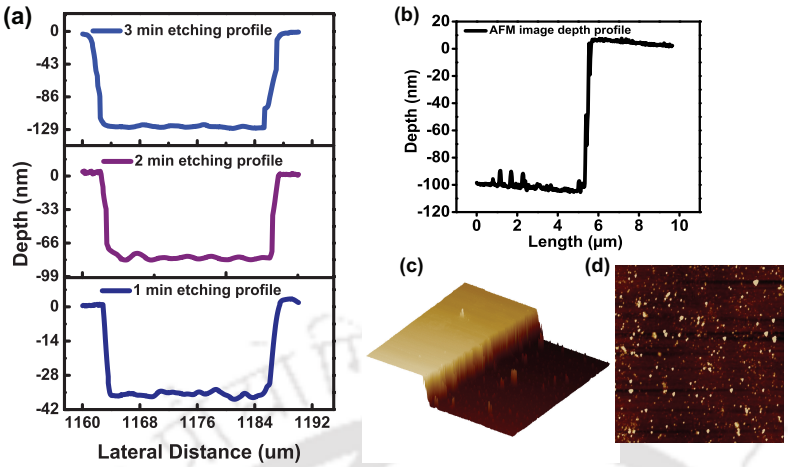

Figure 2.4: (a) Profilometer plots of etched depth profiles, (b) Depth profile of trench from AFM image, (c) 3D AFM image of the trench, (d) AFM image of the etched surface

to be 66.52°. Since the contact angle is less than 90°, the etched surface of SiO_2 can be considered as hydrophilic [77].

Figure 2.4 (a) shows the etched depth profiles of SiO_2 using BOE and glycerine solution in [5:1] ratio after 1 minute, 2 minutes and 3 minutes. Etched profiles are investigated using Profilometer, and the etching rate was 40 nm/min. The hydrophilic nature can be related to surface roughness. Atomic Force Microscopy (AFM) [Make: Bruker] is employed to analyze the etched surface's roughness of SiO_2 (20 μm $\times$ 20 μm) as shown in Figure 2.4 (d). The Arithmetic average roughness (R_a) of 1.67 nm, and root mean squared roughness (R_q) of 2.72 nm are observed. Since the surface roughness was less, the device can be used for liquid-based applications. Figure 2.4 (b) shows the 100 nm AFM image depth profile of SiO_2 trench after 2 minutes and 30 seconds etching. Figure 2.4 (c) shows the well type structure.

2.4.2 Theoretical Consideration of Effective oxide capacitance after etching of SiO_2

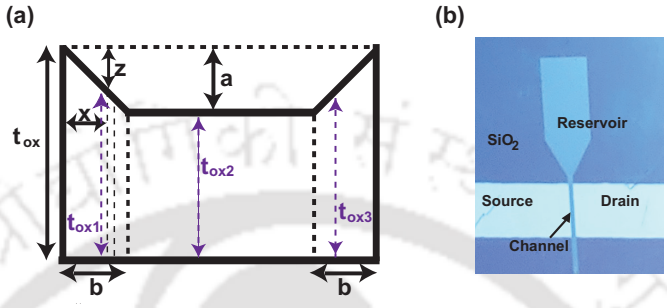

Figure 2.5: (a) Approximated shape of the etched portion, (b) the top view of the fabricated device

Figure 2.4 shows the actual trench and Figure 2.5 (a) shows the approximated trench dimensions and Figure 2.5 (b) shows the top view of the fabricated device. For the cavity we have created, the trench height varies as a function of the position. Since the trench is realized in SiO_2 , this would mean that the oxide capacitance would change as a function of position. For calculating the total effective oxide capacitance, the trench was divided into three regions, having thicknesses, namely t_{ox1} , t_{ox2} and t_{ox3}, as shown in Figure 2.5 (a). We calculated the capacitance of each region.

$$C_{ox} = \frac{\epsilon_{ox}}{t_{ox}} = \frac{\epsilon_r \times \epsilon_o}{t_{ox}}$$

where ϵ_r for $SiO_2 = 3.9$ and $\epsilon_o = 8.854 \times 10^{-12}$ F/m. Therefore, the effective oxide capacitance ($C_{ox_{eff}}$) can be written as

$$C_{ox_{eff}} = \frac{\epsilon_{ox}}{t_{ox1}} + \frac{\epsilon_{ox}}{t_{ox2}} + \frac{\epsilon_{ox}}{t_{ox3}}$$

we can also write it as,

$$C_{ox_{eff}} = C_{ox1} + C_{ox2} + C_{ox3} \tag{2.1}$$

The oxide capacitance in the region of oxide thickness t_{ox2} inside the SiO_2 trench can be defined as

$$C_{ox2} = \frac{\epsilon}{t_{ox} - a} \tag{2.2}$$

To calculate oxide capacitance in other regions, i.e. for $t_{ox1} = t_{ox3}$, we first evaluate the capacitance C_1 for t_{ox1} region using

$$C_{ox1} = \frac{C_1}{\text{Area}} \tag{2.3}$$

The C_1 is the capacitance in Farad and the C_{ox1} is the oxide capacitance per unit area (F/m^2) for the t_{ox1} region. In the t_{ox1} thickness region, we first consider small area of dA taking the small length of dx,

$$dC_1 = \frac{\epsilon dA}{t_{ox} - z}, \text{ where } dA = t_{ox1} \times dx$$

Considering the symmetric triangle,

$$z = a\frac{x}{b}$$

$$\text{we can write } dC_1 = \frac{\epsilon dA}{t_{ox} - z} = b\epsilon\frac{t_{ox1} \times dx}{bt_{ox} - ax}$$

Now for parallel plate capacitor C_1, we integrate dC_1

$$C_1 = \int_{x=0}^{b} dC_1$$

$$= \frac{b\epsilon t_{ox1}}{a}[\ln(\frac{t_{ox}}{t_{ox}-a})]$$

$$\text{Therefore using 2.3, } C_{ox1} = C_{ox3} = \frac{\epsilon}{a}[\ln(\frac{t_{ox}}{t_{ox}-a})] \tag{2.4}$$

Hence from 2.2 and 2.4,

$$C_{ox_{eff}} = 1.32 \times 10^{-4} F/m^2$$

The effective oxide capacitance ($C_{ox_{eff}}$) of the 100 nm depth SiO_2 trench for 20 μm channel length is 1.32×10^{-4}F/m which is more than a standard uniform thick 300 nm SiO_2 by 20%. The 0.01mM of KCl solution also contribute in total capactance by forming the double layer having capacitances of stern layer (C_s) and diffuse layer (C_d) [78, 79]. Therefore total capacitance (C_{total}) is 1.29×10^{-4}F/m^2.

2.4.3 Device Mechanism

Figure 2.6 (a) shows the top view of the fabricated device. The channel is connected to a reservoir having dimensions of 1 mm $\times$ 2 mm $\times$ 100 nm, where 1 μL (approximately) of ionic liquid can placed. The trench dimension was 20 μm $\times$ 2 mm $\times$ 100 nm; therefore, the total amount of liquid that can accommodate inside the trench is 4 pL. The mechanism of the current flow is different in semiconductors and electrolytes. The current in the semiconductor is carried either by holes or electrons, but liquid channel devices are due to ions [45]. The charge carrier

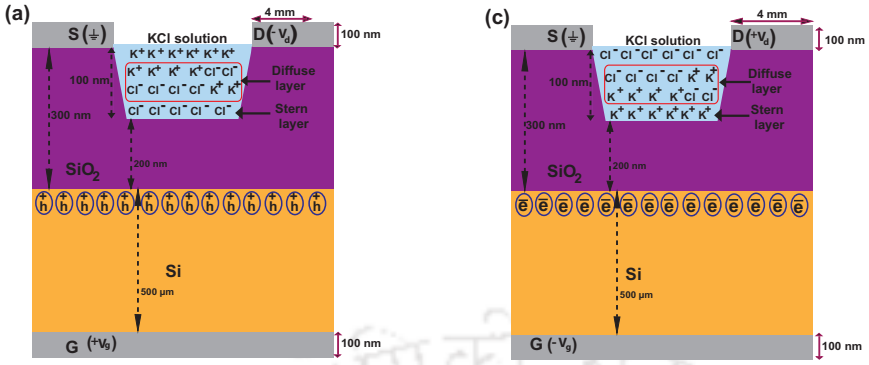

Figure 2.6: (a) p-type device structure with K^+ as ionic channel, (b) n-type device structure with Cl^- as ionic channel

can be positive (anion) or negative (cation) ions in electrolytic (ionic) conduction. DI water does not contain any impurity or ions, but when some salt like KCl is added, the ions in KCl will be dissociated in the water, resulting in a significant electric current. The ions in an aqueous solution are dissociated in the water even if the number of positive and negative ions is close enough. Therefore, they will not get neutralized each other. Since KCl aqueous solution is a strong electrolyte, it is considered one of the most conductive liquids. Strong acids and bases are usually strong electrolytes [80]. Since the microtrench for keeping an ionic liquid is formed between the source and drain, a 0.01 mM KCl solution is kept inside the trench as an ionic liquid channel.

The mobile ions can freely drift under the influence of an electric field resulting in the significant electric current flowing through the solution. Some ions develop the diffuse charge region, extending a few Debye lengths from the insulator/liquid interface into the liquid. One carrier (cation or anion) concentration is more in the channel region and the other decreases upon a gate voltage change. When a positive back gate voltage is biased, the Cl^- will come to a narrow portion of the trench which is closer to Si-SiO_2 interface and form a stern layer. A diffuse layer

is formed by extending the Debye lengths from the SiO_2/liquid interface into the liquid channel as shown in Figure 2.6 (a), and thus form electrical double layer (EDL). Since the K^+ will be on the surface of the liquid channel, it will act as an ionic liquid channel carrier between Source and Drain, and is responsible for current conduction. Similarly, when a negative back gate voltage is biased, the K^+ will form a stern layer at the narrow portion of the trench. Debye length from the SiO_2/liquid interface into the liquid channel is extended and forms a diffuse layer. As shown in Figure 2.5 (b), the K^+ will be closer to Si-SiO_2 interface and thus form electrical double layer (EDL) [81]. In this case, the Cl^- would be the ionic liquid channel carrier between Source and Drain, and wholly responsible for current conduction.

On electrolysis of a solution of potassium chloride, potassium chloride dissociates into K^+ and Cl^-. The anode is connected to positive terminal and cathode to the negative terminal of the battery. So, the oxidation occurs at anode and reduction occurs at the cathode. At the cathode, there are K^+ ions and water. So, while comparing K^+ and H^+ ions, H^+ has greater tendency to get reduced. Hence hydrogen gas is liberated at the cathode, by taking electrons. Similarly, at anode, there are Cl^- and OH^- ions. So, on comparing Cl^- and OH^- ions, oxidation occurs to Cl^-. Hence chlorine gas is liberated by giving electrons to the anode. Hence, there is a continuous source of charge carriers in the liquid channel. The following reactions show electrolysis as well as other side reactions that occur at the anode and the cathode.

Reaction at cathode: Reduction takes place

$$2H_2O + 2e^- \rightarrow H_2(g) + 2OH^-$$

Reaction at anode: Oxidation takes place

$$2Cl^- \rightarrow 2Cl + 2e^-$$

$$2Cl \rightarrow Cl_2(g)$$

Also, the excess ions may probably combine and form H_2O and KCl.

$$H^+ + OH^- \rightarrow H^2O$$

$$K^+ + Cl^- \leftrightarrow KCl$$

Therefore, probably we can say that there is a continuous source of charge carriers in the liquid channel because the electron captured from the cathode will be given to the anode by H^+ and Cl^- ions [82].

With the concentration (c_i) at 25°C for symmetrical charge number (z_i) electrolyte [78], the value of the Debye length (λ_D) is determined by the equation,

$$\lambda_D = \frac{3.04 \times 10^{-6}}{z_i \sqrt{c_i}} \tag{2.5}$$

The calculated Debye length is 96 nm for 0.01 mM KCl, which is slightly lower than the depth of the SiO_2 trench.

2.4.4 Electrical Characteristics

Using dc probe station and Keithley 4200 parametric analyzer device characterization was carried out.

The drain and source electrodes are connected through the liquid channel. The conductivity is possible only if an adequate amount of liquid is present in the channel because then only a connection will be established between the source and the drain. This is illustrated in Figure 2.7 (a), which shows that the current is very minimal when less amount of ionic liquid is kept inside the trench. However, the

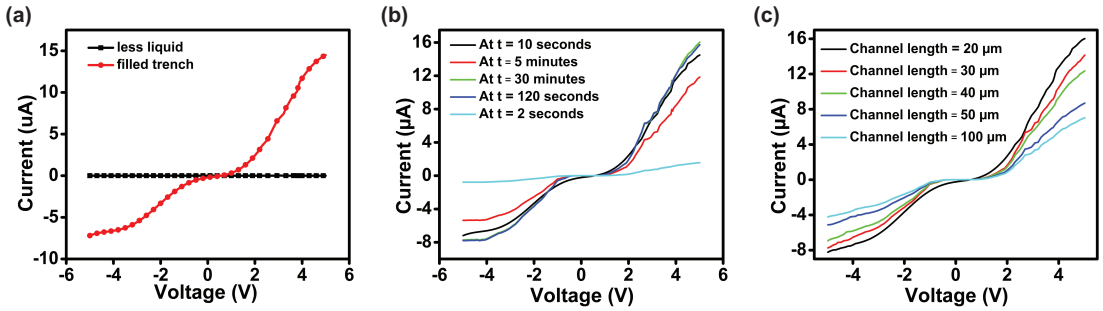

Figure 2.7: (a) IV characteristics showing the current flow when less volume of liquid is kept and with sufficient liquid in the trench in the trench, (b) IV characteristics with sufficient liquid in the trench at different time, (c) IV characteristics with different channel length at t = 10 s

current is higher when the trench is filled with ionic liquid. An ionic liquid first fill in the reservoir and subsequently, the liquid is transferred to the channel region naturally. The arrangement is shown in Figure 2.5 (b). We have performed the I-V characteristics at different time intervals soon after filling the reservoir with the liquid. Figure 2.7 (b) shows changes in IV characteristics up to 120 seconds, at t = 2 s, the current is negligible since it takes few seconds to get the channel trench filled with the liquid from the reservoir. At t = 5 s, the current flow gradually starts. It indicates that beyond 10 s seconds, the current is almost constant. It may be concluded that it would take a set-up time of 10 seconds to get the channel trench filled for this device arrangement. The volume of liquid could increase by increasing the channel length, but the device's resistance will increase, reducing the transconductance (Figure 2.7 (c)). Therefore, we set the channel length to 20 μm. However, if the depth of the trench increases, there may be an improvement in the device performance, which we would take it up as future work.

Subsequently, the I-V measurement of device was taken with a 0.01 mM KCl ionic solution and glycerine solution of [1:1] ratio as an ionic liquid channel to avoid evaporation while taking the ionic current characteristics. First of all, the I-

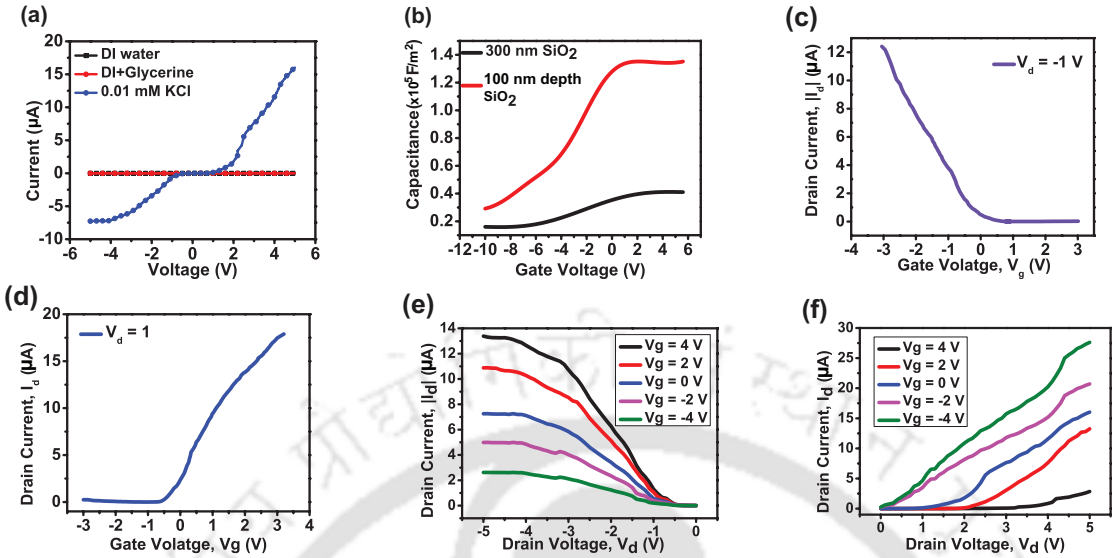

Figure 2.8: (a) I-V characteristics for DI water, DI mixed with Glycerine , 0.01 mM of KCl, (b) C-V characteristics, (c) Transfer Characteristics of K^+ as an ionic channel (p-FET), (d) Transfer Characteristics of Cl^- as an ionic channel (n-FET), (e) Output Characteristics of K^+ as an ionic channel (p-FET), (f) Output Characteristics of Cl^- as an ionic channel (n-FET)

V characteristics of DI water, DI water and glycerin [1:1] are checked as a baseline, and it was negligible as it comes in the range of 10 fA as shown in Figure 2.8 (a). Conductivity is very sensitive to concentration, temperature, viscosity variations. However, mild changes in environmental conditions such as humidity and pressure will not affect the ionic conductivity. The C-V characteristics of the 100 nm depth SiO_2 trench of an area $4 \times 10^{-8}m^2$ as a function of the bias voltage at 1kHz is 1.3 $\times$ $10^{-5}F/m^2$. The experimental value of C_{ox} is more than the theoretical value of C_{ox}. This may be due to some area apprroximation errors. The improvement in C_{ox} of trench structure compared to the uniformly thick SiO_2 is clearly seen in Figure 2.8 (b).

For transfer characteristics, our device was biased in both n-FET for Cl^- as ionic liquid channel and p-FET for K^+ as an ionic liquid channel at drain voltages of 1 and -1 V, respectively. For p-FET transfer characteristic, Figure 2.8 (c)

shows that drain current increases sharply for V_d = -1 with I_{ON}/I_{OFF} ratio of 10^5. Similarly for n-FET transfer characteristic, the drain current increases sharply for $V_d = 1$ with I_{ON}/I_{OFF} ratio of 10^5 as shown in Figure 2.8 (d). The threshold voltage for both the p-FET and n-FET are estimated using Linear Extrapolation (LE) method in the linear region [83, 84]. In this method, the V_g axis intercept point is defined from the maximum first derivative (slope) of the linear extrapolation of the I_d–V_g curve. Then, $V_d/2$ is added to the resulting V_g axis intercept, and hence the resulting value is threshold voltage (V_t). The calculated threshold voltages are 0.8 V and -1.2 V for nFET and pFET respectively. The transistor transconductance (gm) at a drain voltage of -1 V was 2.9×10^{-6}S for pFET and 6.4×10^{-6}S for nFET at 1 V.

For mobility calculation, as a first step we establish in the Justification below the following relation between an ion's mobility and its molar conductivity [85]:

$$\lambda = z\mu F \tag{2.6}$$

where F is Faraday's constant ($F = N_A e$), z = valency, μ= mobility.

At Gate voltage, V_g = -3 V, Drain current, I= 1.2×10^{-5} , Resistance, R= 250 KΩ.

For device area calculation, Channel length, L=20 μm, Channel width, W= 2 mm, thickness = 100 nm

Conductivity = L/(RA) = 0.4 S/m

Molar conductivity, λ = (conductivity)/Molarity = 40 Sm^2mol^{-1}

Molar conductivity of K^+ ions from calculation is 40 S m^2/mol, so from the equation the value of mobility

$$\mu = \frac{\lambda}{zF} \tag{2.7}$$

$$= \frac{40}{1 \times 6.022 \times 10^{23} \times 1.6 \times 10^{-19}} = 4.15 \times 10^{-4}$$

Similarly, Chlorine ion (Cl^-) mobility, At Gate voltage, V_g = 3 V, Drain current, I= 1.83 x 10-5 A, Resistance, R= 163 KΩ.

Conductivity = L/(RA) = 0.61 S/m

Since we are considering the KCl solution as channel material, we again calculate the Molar conductivity, λ = (Conductivity)/Molarity = 61 Sm^2mol^{-1} For Cl- the value of mobility

$$\mu = \frac{\lambda}{zF} = \frac{61}{1 \times 6.022 \times 10^{23} \times 1.6 \times 10^{-19}} = 6.33 \times 10^{-4}$$

Since our KCl solution is a strong electrolyte of a fully dissociated at a molar concentration of 0.01 mM. Current and potential difference are related by Ohm's law, V = IR, so it follows that

$$I = zvcqN_A\mu A\frac{V}{L}$$

Where z = valency, v = number of ions, c = molar concentration, q = charge, NA= Avogadro's number, A = area, V= voltage, L = channel length

Considering each formula unit give rise to v^+ cations of charge z^+e and v^- anions of charge z^-e. The molar concentration of each type of ion is therefore vc (with v = v^+ or v^-), and the number density of each type is vcN_A As each KCl molecule have one K^+ and one Cl^- ion, hence total number density of each type of ion is=vcNA= $1 \times 0.01 \times 6.022 \times 10^{23} = 6.022 \times 10^{21}/m^3$.

For K^+ ions,

$$\mu = \frac{IL}{zvcqN_AAV} = \frac{1.2 \times 10^{-5} \times 20 \times 10^{-6}}{1 \times 1 \times 0.01 \times 1.6 \times 10^{-19} \times 6.022 \times 10^{23} \times 2 \times 10^{-10} \times 3}$$

$$\mu = 4.15 \times 10^{-4}$$

For Cl^- ions,

$$\mu = \frac{IL}{zvcqN_AAV} = \frac{1.83 \times 10^{-5} \times 20 \times 10^{-6}}{1 \times 1 \times 0.01 \times 1.6 \times 10^{-19} \times 6.022 \times 10^{23} \times 2 \times 10^{-10} \times 3}$$

$$\mu == 6.33 \times 10^{-4}$$

Therefore, the mobility values calculated from the molar conductivity and ohm's law have same values mobilities of each ion. This indicates that the mobility is improved as compared with other works [45, 47]. The increase in effective oxide capacitance enhances the transconductance of the device. Hence mobility increases in our case. The mobility of ions in the liquid depends on various factors such as ionic concentration, electric field strength, and interaction between the hydrated ion pairs etc. [86, 87, 88]. The mobility also depends on the size of the ion, but a smaller ion has higher hydration because smaller atoms can accommodate a large number of water molecules around it and get highly hydrated. Therefore, less size hydrated ions have higher mobility [87]. According to Debye, Huckel, and Onsager (DHO), various forces acted on the moving ion, such as relaxation, electrophoretic, and frictional forces, which arise due to various interactions between ions or ions and solvents. Therefore, the concentration rises, the mobility of ions decreases

Table 2.3: Comparison of ionic liquid channel Field effect transistor

Substrate	**Channel**	**Electrode**	**Channel architecture**	**gm**	**Mobility (m^2/Vs)**	Ref.
Pyrex	Na^+	Pt	Nano-channels of plasma etched	$4-8\times10^{-6}$S	36×10^{-8}	[48]
Si	KCl, H_3BO_3	Cu, Au	Capillary channel	-	For KCL 8.49×10^{-11}	[45]
Si	KCl	Ag/AgCl	Nano channel array	-	$K+ = 7.62\times10^{-8}$ $Cl- = 7.92\times10^{-8}$	[89]
Glass	KCl	ITO, Au	400 um channel length	30 nS	1×10^{-4}	[47]
Si	KCl	Ti, Au	Nan o-dimensioal fluidic channel	-	$K+ = 7.62\times10^{-8}$ $Cl- = 7.92\times10^{-8}$	[49]
Si	KCl	Cr, Au	Nano channel	-	$K+ = 7.62\times10^{-8}$ $Cl- = 7.92\times10^{-8}$	[52]
Si	**KCl**	**Al**	**20 μm length microtrench structure inside SiO_2 with back gate**	**p-FET = 2.9×10^{-6}S n-FET = 6.4×10^{-6}S**	**$K^+ = 4.15\times10^{-4}$ $Cl^- = 6.33\times10^{-4}$**	**[90]**

because the scattering or collisions of ions will occur. In the present study, 0.01 mM of KCl was used as an ionic liquid, a minimal concentration. When the gate voltage is applied, the ions are separated. Only one type of ion is formed on the top side and wholly responsible for current conduction. Hence, the effective concentration is halved; the interaction between ions is reduced, and therefore, mobility increases [87]. Figure. 2.8 (e)-(f) shows the graph of the drain current versus drain voltage for different gate voltage values of our proposed device. For p-type output characteristic curves, the positive gate voltage makes Cl^- comes to

Table 2.4: Calculation of number of ions from electrical characteristics

Parameter	**0.01 mM KCl solution**	
Ion	K^+	Cl^-
Conductivity (S/m)	2×10^{-3}	3.08×10^{-3}
Molar conductivity (Sm^2mol^{-1})	0.2	0.308
Calculated number of ions	9.5×10^{20}	9×10^{20}
Number of ions in solution	1.2×10^{19}	1.3×10^{19}

a narrow portion of the trench and creates an accumulation of K^+ in the channel, and increases the drain current as shown in Figure 2.8 (e). A drain current of 13.5 μA was exhibited at a gate voltage of 4 volts and a drain voltage of -5 volts. The current is increased as the positive gate voltage is increased because more Cl^- will come to the SiO_2 interface as positive gate voltage increases and more K^+ accumulates in the channel region between the source and drain electrode. Similarly for n-type output characteristic curves as shown in Figure 2.8 (f), the negative gate voltage makes K^+ comes to a narrow portion of the trench and creates an accumulation of charges (Cl^-) in the channel, and increases the drain current. The current is increased as the negative gate voltage is increased. A drain current of 27 μA was exhibited at a gate voltage of -4 volts a drain voltage of 5 volts. Since more the negative gate voltage, more K^+ will come to the SiO_2 interface, and more Cl^- accumulates in the channel area between the source and drain electrode. Table 2.3 shows the comparison of our work with different parameters reported. Our devices show good performance as compared with others in those calculated parameters.

The numbers of Cl^- and K^+ are calculated from the I-V graph (Figure 2.8 (c-d)) and compared with the number of ions in molar solutions. Table 2.4 shows the comparisons between number of ions in molar solution and the calculated number of ions. The value of the experimentally calculated ion is somewhat more

than the calculated number of ions from molarity. This may be attributed to the purity of KCl (99%). That 1% of impurity includes heavy metals (Pb), Iron (Fe), and Magnesium (Mg). The 1% number of ion in impurities is calculated using their molecular mass, and it was 1.85×10^{17} which may take part in the electrical characteristics. Also, since the measurement was done at room temperature in an open chamber, other ions may also involve in the measurement.

2.5 Summary

This chapter shows the fabrication of a 100 nm deep liquid container in SiO_2 using photolithography and selective etching. The depth of the SiO_2 trench was estimated using a Profilometer, and the etched surface was characterized using the contact angle method and AFM. Theoretically, effecetive oxide has been calculated, and the obtained value was 20 % more than the uniformly doped SiO_2. The electrical properties of the FET characteristic have been measured and have obtained both n-FET and p-FET characteristics depending upon the back gate biasing conditions. This chapter proposed a simple liquid channel FET excluding any other mold or liquid containing intricate architecture, which can further be used for many bio-sensing applications.

Chapter 3

DETECTION OF H_2O_2 USING rGO/ PPy NANOCOMPOSITE

3.1 Introduction

This chapter demonstrates the high-performance hydrogen peroxide ((H_2O_2)) sensing field-effect transistor (FET) using reduced graphene oxide - polypyrrole (rGO/PPy) nanocomposite. The SiO_2 trench type FET is fabricated using lithography and etching techniques. The fabricated SiO_2 trench structure was used not only for holding (H_2O_2) but also for sensing purpose. Biological processes including food science, environmental monitoring, healthcare and pharmaceutical science require hydrogen peroxide (H_2O_2) detection [91, 63, 92, 93]. Various methods of H_2O_2 detection such as spectroscopic, electrochemical, colorimetric, Field-effect transistors (FETs) based and fluorescence-based have been studied [94, 95, 96, 97, 63]. There are also other detection strategies for hydrogen peroxide, such as photoelectrochemical method and non-enzymatic electrochemical method [98, 99]. Among all types of H_2O_2 sensor, Field-effect transistor (FET) based is the most attractive because of its amplification ability of output current [100, 101].

In this work, our focus was to develop hybrid materials using a simple synthetic method and improve the sensing performance. We developed a high-performance H_2O_2 sensor using rGO/PPy nanocomposite SiO_2 trench embedded Field effect transistor (FET). The FET characteristics would show p-type FET behavior because of the hole transport resulting from the rGO/PPy nanocomposite which absorb oxygen and water from the air [102, 103]. The rGO/PPy nanocomposite is expected to show enhanced conductivity and results in good sensing performance because PPy NPs will be acting as conductive channel sandwiched between rGO layers. We have initially demonstrated this enhanced sensing performance of rGO/PPy in the cyclic voltammetry (CV) study. The material characterization of the rGO/PPy nanocomposite has been done to analyze their structure and morphology. The response intensity was investigated as a function of the concentration of H_2O_2. Further, the signal-to-noise and the limit of detection were obtained, and the values were compared to already reported H_2O_2 sensors. The proposed structure has a SiO_2 trench along with a reservoir that removes the need for any extra mould for containing the analyte liquid. However, the inbuilt trench structure add a few more benefits which are as follows: 1) The trench, along with the reservoir structure, can ease the analyte pouring during the sensing. Also, it helps in case storage of liquid is required; 2) It helps in minimizing the overflow of the analyte liquid, which is a major cause of electrode degradation and sensor failure; and 3) Trench structure brings an increment in effective oxide capacitance, which improves gate control [104].

3.2 Materials and Method

3.2.1 Materials

Graphite powder, Sodium nitrate ($NaNO_3$), Potassium permanganate ($KMnO_4$), Sulfuric acid (H_2SO_4), Hydrogen peroxide (H_2O_2), Hydrochloric acid (HCl), Polypyrrole (PPy), 2-propanol, ethanol, methanol and ITO coated PET were purchased from Sigma Aldrich, India. Phosphate buffered saline (PBS) was obtained from SRL, India. Phosphorous doped of $< 100 >$ oriented Si wafers of 500 μm thick with 300 nm of SiO_2 were purchased from University Wafer. The Milli-Q grade water was used in all the experiments.

3.2.2 Preparation of Materials

The graphene oxide (GO) is synthesized using the modified Hummers method [105]. For rGO, the hydrazine hydrate of 1 mL was added in GO suspension (100 mL, 1 mg mL^{-1}), and the solution was heated in the water bath at 90 ° C for 2 hours. This product was isolated by filtration, washed many times with DI water and methanol, and dried at 50 ° C in vacuum [106].

0.1 mg of rGO were mixed with 1 mL of Ethanol and 0.1 mg of PPy is also mixed with 1 ml of Ethanol seperately. Then each solution is ultrasonicated for 1 hour. For rGO/PPy nanocomposite synthesis, we made [1:1] ratio of rGO:PPy which is 100 μL of rGO and 100 μL of PPy and sonicated for 30 mins.

3.2.3 Fabrication of Hydrogen peroxide sensing device

For the fabrication process flow, we followed the same procedure as we mentioned in chapter 2, section 2.3. After the device was fabricated successfully, the

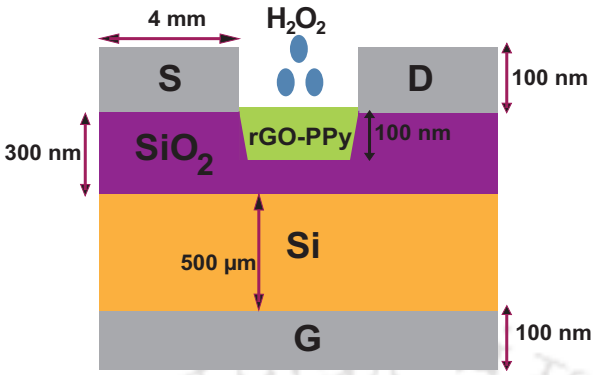

Figure 3.1: The cross-sectional (schematic) view and top view of the fabricated device

rGO/PPy nanocomposite was dropcasted as an active channel material for the detection of H_2O_2. Once the channel region was filled with dropcasted material, it was dried and annealed on a hotplate at 135° C for 30 minutes. The hotplate's temperature is then gradually reduced to room temperature. The device was then placed in a desiccator to protect it from the environment's damaging impacts. Figure 3.1 shows the schematic side view of the device.

3.3 Results and Discussions

3.3.1 Material characterisation

To ensure the formation of chemical bonds between the rGO and PPy nanocomposite, material characterization with different instruments were performed. Raman analysis was performed in Horiba LabRam HR Evolution Raman spectrophotometer, USA. Fourier transform infrared (FTIR) spectra were acquired using a PerkinElmer spectrometer. Field Emission Scanning Electron Microscope (FESEM) imaging was also performed for surface morphology of the nanocomposite using FESEM. X-ray powder diffraction (XRD) analysis was done to check the

crystallinity of the materials.

FESEM Analysis

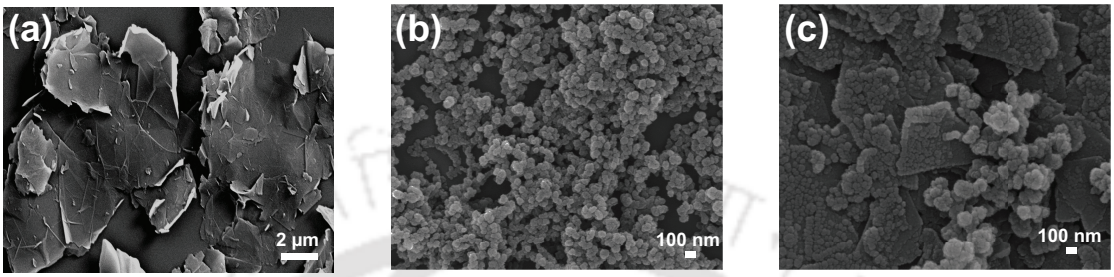

Figure 3.2: FESEM images of (a) rGO, (b) PPy, (c) rGO/PPy nanocomposite

The morphologies of rGO, PPy and rGO/PPy nanocomposite was analysed using FESEM images shown in Figure 3.2. (a) The FESEM image of rGO sheets, (b) FESEM image of PPy nanoparticles, and (c) The FESEM image of rGO/PPy nanocomposite material shows interactions of PPy nanoparticles with the rGO sheets. The PPy nanoparticles structure was thoroughly organized on the rGO sheets's surface area. The associated interactions and stability of the rGO/PPy nanocomposite can be understood from the following discussions.

Raman Analysis

Raman study was carried out to look into the structures of rGO/PPy nanocomposite and the results are plotted in Figure 3.3 (a). The rGO Raman spectrum shows two prominent bands at 1352 cm^{-1} and 1601 cm^{-1} corresponding to D bands and G bands. For the PPy Raman spectrum, peak at 1380 cm^{-1} shows the C=C backbone, and at 1577 cm^{-1} shows the ring stretching mode of PPy. For rGO/PPy nanocomposite, at around 1348 cm^{-1} of Raman spectra, the band's increased intensity indicates an interaction between PPy and the rGO sheets forming a composite.

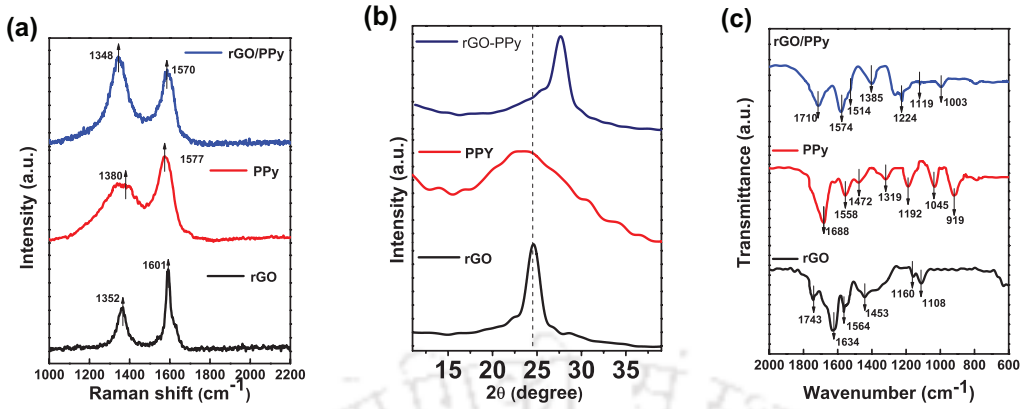

Figure 3.3: (a) Raman spectra of rGO, PPy and rGO/PPy nanocomposite, (b) XRD pattern of rGO, PPy and rGO/PPy nanocomposite, (c) FTIR spectra of rGO, PPy and rGO/PPy nanocomposite

XRD Analysis

Figure 3.3 (b) shows the XRD pattern for rGO, PPy and rGO/PPy composite. A broad peak appeared at 24.6° [107] implies that rGO is formed. The PPy shows a broad peak of amorphous characteristic at about $2\theta = 23°$ [108, 109]. For rGO/PPy composites, the peak shifted to $2\theta = 28°$ due to the interaction of $\pi - \pi$ stacking between rGO sheets and PPy [110].

FTIR Analysis

The FTIR spectra for rGO, PPy, and rGO/PPy nanocomposite were recorded, and are shown in Figure 3.3 (c). For rGO, the $C - O$ stretching band at 1108 cm^{-1}, $C - O - C$ stretching at 1160 cm^{-1} are observed. The band at 1453 cm^{-1} represents $C - OH$, 1564 cm^{-1} corresponds to sp^3 $C - C$ stretching, 1634 cm^{-1} corresponds to $C = C$ stretching, and at 1743 cm^{-1} corresponds to a carbonyl group. The FTIR of PPy show stretching vibration ($C = O$) at 1688 cm^{-1}, pyrrole rings stretching vibration at 1558 and 1472 cm^{-1}, deformation vibrations ($C - H$) at 1045 cm^{-1}, stretching vibrations ($C - N$) at 1319 cm^{-1}, and bipolaron at 1192 and 919 cm^{-1} [66]. For rGO/PPy nanocomposite, the peaks at 1574 and 1224

cm^{-1} are due to the C = C and –OH. The peaks at 1710 and 1385 cm^{-1} correspond to the shifted carbonyl (C = O) and carboxy (C–O) stretching vibrations which obtained from the $\pi - \pi$ interaction between rGO sheets and PPy nanoparticles. Further, the formation of rGO/PPy represent by the peaks at 1003, 1119, 1514 cm^{-1} which correspond to $N - H$ out-of-plane bending of PPy, C–N stretching, and N–H bending [110].

3.3.2 Electrochemical detection of H_2O_2 by cyclic voltammetry

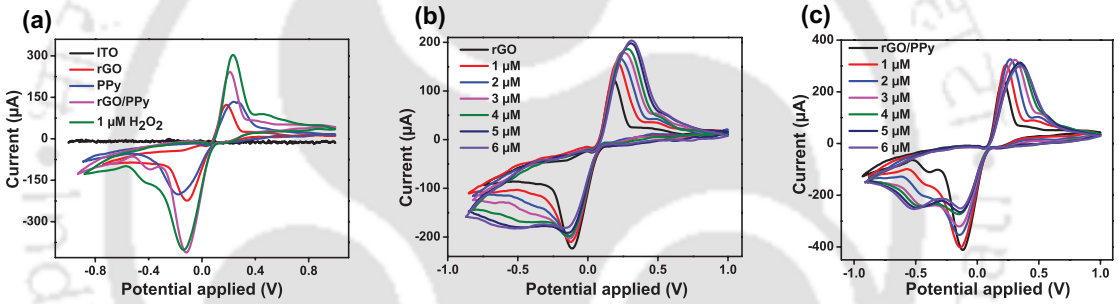

Figure 3.4: (a) Cyclic voltammograms of ITO, rGO-modified ITO coated PET, PPy-modified ITO coated PET, rGO/PPy-modified ITO coated PET, and 1 μM of H_2O_2 sensing by the rGO/PPy-modified ITO coated PET, (b) Cyclic voltammograms of rGO modified ITO coated PET as a function of H_2O_2 concentration from 1 to 6 μM, (c) Cyclic voltammograms of rGO/PPy modified ITO coated PET as a function of H_2O_2 concentration from 1 to 6 μM

Electrochemical detection of H_2O_2 using cyclic voltammetry with rGO, rGO/PPy nanocomposite was performed first to validate the sensing ability. The Figure 3.4 (a) shows the cyclic voltammetry graph changes of ITO, rGO, PPy and rGO/PPy with ITO electrode in the 0.1 mol L^{-1} solution of PBS at 20 mV s^{-1} scan rate.

Figure 3.4 (b) shows the cyclic voltammetry graph changes of the rGO with ITO electrode for different H_2O_2 concentration of 1 μM to 6 μM in the solution of 0.1 mol L^{-1} PBS at 20 mV s^{-1} scan rate. In the absence of H_2O_2 in a typical

rGO with ITO electrode, oxidation and reduction peaks are observed. With the addition of H_2O_2 concentration, the cathodic and anodic peak current changes proportionate to H_2O_2 concentration. It was observed that in the absence of H_2O_2, anodic peak of rGO ITO electrode appears at 0.19 V while in presence of 1 μM H_2O_2, the peak was shifted to more positive potential 0.22 V. Initially, the cathodic current at -0.56 V is 86 μA and when H_2O_2 added in increment of 1 μM in PBS solution, it is increased to 102 μA, 115 μA, 118.45 μA, 128.59 μA, 153 μA 174 μA and 185 μA. Figure 3.4 (c) shows the changes in cyclic voltammetry graph of the rGO/PPy nanocomposite with ITO electrode of with different H_2O_2 concentration 1 μM to 6 μM in the solution of 0.1 mol L^{-1} PBS at 20 mVs^{-1} scan rate. Initially, a typical rGO/PPy composite in ITO electrode oxidation and reduction peaks were observed. With the addition of H_2O_2, the cathodic peak current and anodic peak current change accordingly with the changes of the H_2O_2 concentration. It was observed that in that initally the anodic peak of rGO/PPy ITO electrode appears at 0.20 V and when 1 μM of H_2O_2 was added, the peak was shifted to more positive potential 0.23 V. Increasing the concentration of H_2O_2 from 1 μM to 6 μM has shifted the peak to more positive potential (0.26 V, 0.30 V, 0.33 V, 0.345 V and 0.35 V) with increasing width of each peak. The additional cathodic shoulder peak at -0.41 V is the peak corresponding to the rGO/PPy and its peak shifted to more negative side increasing the reduction current when H_2O_2 concentration increases. The cathodic current initially at -0.55 V is 68.48 μA and then when H_2O_2 added in increments of 1 μM in PBS solution, it was increased to 100.18 μA, 143.9 μA, 194.45 μA, 215.59 μA, 233 μA and 245 μA. These observations indicate that the shift in peak potentials and the increasing of shoulder peaks (cathodic current) are direct consequences of H_2O_2 interaction with electrode and/or rGO/PPy. The rGO/PPy nanocomposite is selected as an

active channel material for the fabricated device, since its sensing current of H_2O_2 is higher than rGO alone case.

3.3.3 Electrical Characteristics of H_2O_2 FET Based Sensors

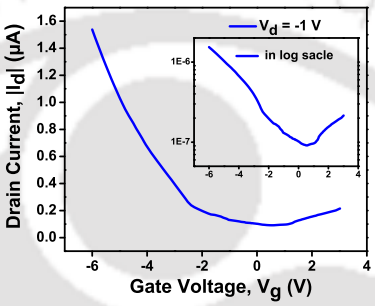

Figure 3.5: Transfer characteristic of rGO/PPy nanocomposite

The rGO/PPy nanocomposite is used as a conductive channel material to investigate the H_2O_2 detection as FET characteristics. We measured the transfer characteristics of the device ($I_D - V_G$) as shown in Figure 3.5 at V_D = -1 V. Further, we measured the output current-voltage ($I_D - V_D$) characteristics to investigate the electrical characteristics of the rGO/PPy nanocomposite's conductive channels at various gate biases. Figure 3.6 (a) shows typical characteristics of p-channel transistors where I_D increases with negative gate bias. It indicates that the device's current was due to hole transport which also shows that the hole carrier density at the surface of rGO/PPy nanocomposite controls the modulation of I_D. PPy material is well known for its p-type semiconductor behavior. The rGO absorb oxygen or water from the air and exhibit hole-transporting behavior to produce rGO/PPy nanocomposite that behave as enhanced p-type characteristics.

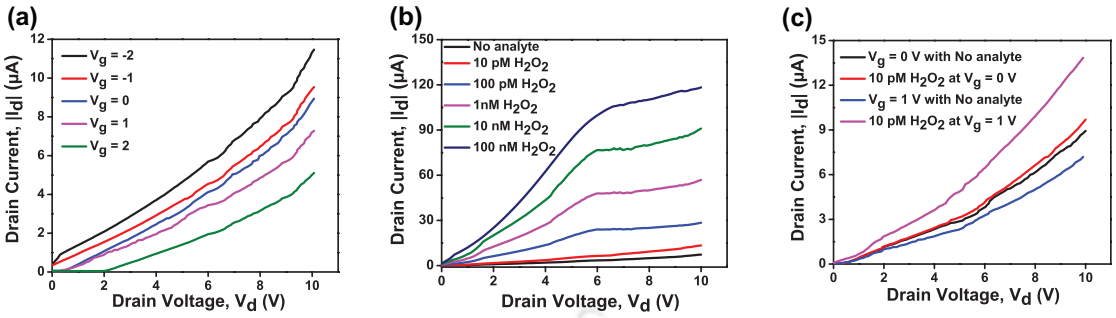

Figure 3.6: (a) Output Characteristic at various V_g range, (b) Output Characteristic at V_g = 1 V, (c) Output Characteristic of 10 pM H_2O_2 at V_g = 0 V and V_g = 1 V

For the measurements of various concentration of H_2O_2, the gate voltage (Vg) was kept at 1.0 V as shown in Figure 3.6 (b). The output current increases significantly when the concentration of H_2O_2 increases. Figure 3.6 (c) clearly indicates that the change in device characteristics for 10 pM H_2O_2 is minimal when no gate voltage is applied. However, when a gate terminal is biased at 1 V, the current is enhanced. Therefore, the limit of detection could be improved using our fabricated back gated device.

3.3.4 Transient Response of various H_2O_2 concentration

By varying the concentrations of H_2O_2, the real-time response was characterized using our fabricated p-type FET sensor at Vg = 1. The drain current (I_D) changes are measured with respect to the variation of H_2O_2 concentration. Since there is accumulation of p-type charge carriers at the rGO/PPy nanocomposite surface, the drain current (I_D) increases gradually as the concentration of H_2O_2 increases (Figure 3.7 (a)). SiO_2 trench FET device using rGO/PPy nanocomposite exhibit susceptible responses to H_2O_2, with a detection limit of approximately 10 pM. The signal-to-noise ratio (S/N) higher than or equivalent to 3.0 is usually considered a significant signal [15, 111]. The signal-to-noise ratio of 10 pM is 3.22 which is

considerable.

3.3.5 Selectivity

The specificity of the proposed device was thoroughly studied. Uric acid, Ascorbic acid, Glucose, Galactose, Sucrose, and urea molecules were considered due to their similar nature. The sensor's response was estimated towards them and compared against hydrogen peroxide in (Figure 3.7 (b)). It can be concluded from the (Figure 3.7 (b)) that the proposed sensor is highly specific towards hydrogen peroxide.

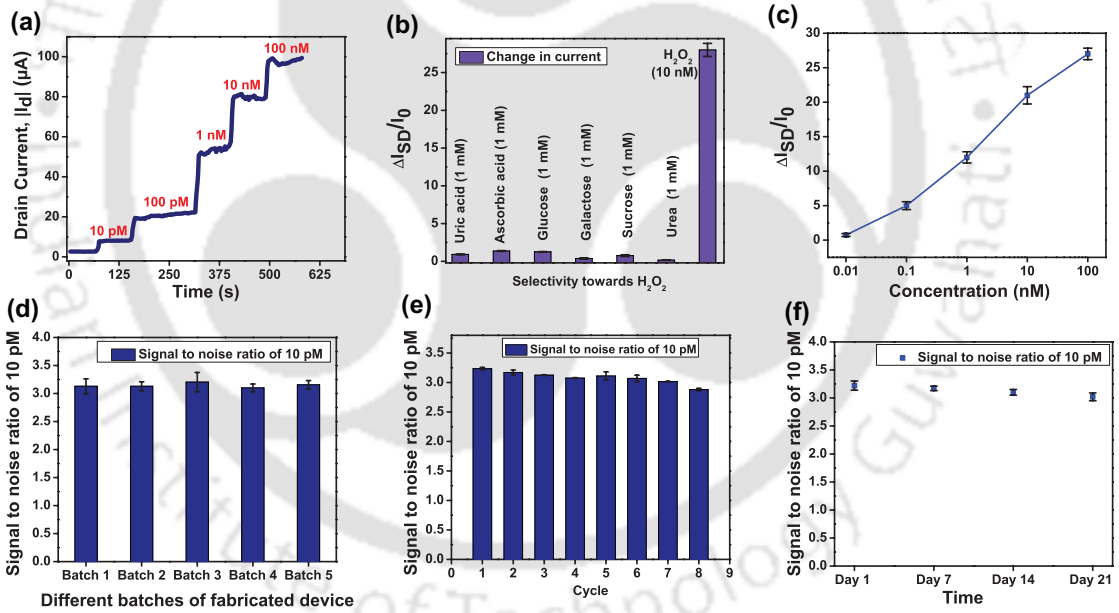

Figure 3.7: (a) Transient response of rGO/PPy nanocomposite based H_2O_2 sensor, (b) Selectivity towards H_2O_2, (c) Sensitivity curve for H_2O_2 based on rGO/PPy nanocomposite were measured at Vd = 6 V (Vg = 1 V) with H_2O_2 concentrations of 10 pM to 100 nM, (d) Signal to noise ratio for 10 pM H_2O_2 of different batches of fabricated devices, (e) Signal to noise ratio for 10 pM H_2O_2 of single fabricated device in several cycles, (f) Signal to noise ratio curve for 10 pM H_2O_2 in several days

Table 3.1: Cross sensitivity of hydrogen peroxide with other biological fluids

Fluid	**Molarity**	**Sensitivity**
Uric acid (UA)	1 mM	1.22
Ascorbic acid (AA)	1 mM	1.37
Glucose	1 mM	1.26
Galactose	1 mM	0.38
Sucrose	1 mM	0.76
Urea	1 mM	0.16
H_2O_2	10 nM	27

3.3.6 Sensitivity

When the H_2O_2 concentration is increased, higher level of electrical signals were detected. From the normalized change in the current, the sensitivity was determined using following equation

$$\frac{\Delta I_{SD}}{I_0} = \frac{(I_{SD} - I_0)}{I_0} \tag{3.1}$$

where I_0 is the base current and I_{SD} is the measured current of individual concentration of H_2O_2. Figure 3.7 (c) shows the response current (I_{SD}) increases gradually with the increase in concentration of H_2O_2 due to the charge accumulation at rGO/PPy nanocomposite's surface. Table 3.1 describes the sensitivity acheived by the H_2O_2 against other biological fluids.

3.3.7 Repeatabilility

For any biosensing device, precise repeatability is the basic requirement across multiple fabrications. To check the repeatability of device performance, I–V characteristics of 10 pM H_2O_2 sensing are conducted across different batches of fabricated devices with the same specification. Figure 3.7 (d) shows the measured

Table 3.2: Performance comparison of the Various Hydrogen peroxide Sensors

Material	**Configuration**	**Response Time**	**Detection limit**	**Year**	**Ref**
rGO/PPy NT	Liquid gated FET	1 s	100 pM	2014	[63]
Melanin-Capped Fe^3+, Cu^{2+}, or Ni^{2+} Modified Prussian Blue Nanoparticles	Cyclic voltammetry	NA	0.14, 0.32, and 0.57 uM	2015	[91]
PPy NWs/Cu/Au electrode	Cyclic voltammetry	5 s	2.3 uM	2018	[62]
MoS2/RGO	Liquid gated FET	$<$ 1 s	1 pM	2019	[112]
Cyt c/graphene	Liquid gated FET	$<$ 1 s	100 fM	2020	[113]
rGO/PPy nanocomposite	**SiO_2 trench FET with back gate**	**5 s**	**10 pM**	**2021**	**[114]**

signal to noise ratio of 10 pM H_2O_2 for each device at fixed gate and drain bias. The variation of batch-to-batch is within $\pm$0.95 % of the mean reading.

To study the reusability of the sensor, we have considered a single device. The 10 pM of H_2O_2 sensing is found to be degraded from the eighth cycle onwards as shown in Figure 3.7 (e). This may be due to multiple washes of the channel layer. The signal-to-noise ratio is more than three for 10 pM H_2O_2 till the seventh measurement without significant variation. However, in the eighth measurement, the S/N signal reduces below three and thus cannot be considered assuredly as sensing of 10 pM H_2O_2.

3.3.8 Stability

The response time obtained for our SiO_2 trench FET-type sensor, 5 s, is comparable to other H_2O_2 sensors, as shown in Table 3.2. Our device indicates good reproducibility with no change of response after repeated experiments. Also, de-

vice shows high stability in the detection of H_2O_2. As shown in Figure 3.7 (f), the signal to noise ratio of 10 pM H_2O_2 of freshly prepared device is 3.22. A value greater than 3 is acceptable and the obtained values were 3.17, 3.1 and 3.02 once these devices were retested after 7, 14 and 21 days, respectively for 10 pM H_2O_2.

3.3.9 Sensing Mechanism

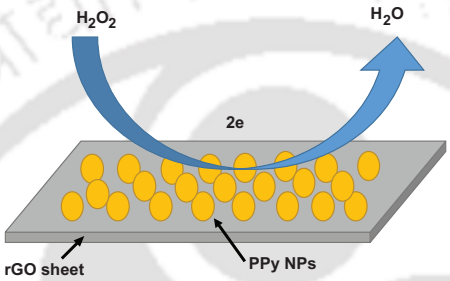

Figure 3.8: Sensing mechanism

The proposed sensor has a composite of rGO and PPy as a sensing layer. Both rGO and PPy possess strong interaction and catalytic activity towards oxygen atoms. Therefore, they are used in oxygen reduction reactions (ORR) and even in oxygen evolution reactions. As shown in Figure 3.8, the hydrogen peroxide added during the sensing experiments gets decomposed; the reaction is given as follows:

$$H_2O_2 \rightarrow H_2O + O_2$$

The generated oxygen atoms get adsorbed over the rGO/PPy composite. The cyclic voltammetry analysis shows that the rGO layer current increases as the concentration of $H_2O + O_2$ increases. However, after introducing the PPy NPs to the rGO layer, the sensing current enhances. The sensing of $H_2O + O_2$ using rGO/PPy nanocomposite showed more electrical signal changes than rGO alone. This observation is because both rGO and PPy possess strong interactions with

oxygen atoms and PPy nanoparticles over rGO effectively improve the surface area (surface to volume ratio). Therefore, the adsorption is improved in the composite and the increment in current is more.

Also, in fabricated FET device, the applied gate bias for sensing ($V_g = 1V$) was kept smaller than the H_2O_2's oxidation potential in order to avoid electrochemical oxidation of H_2O_2; hence it can be said that the changes in I_{SD} did not happen due to electrochemical oxidation of H_2O_2. In summary, H_2O_2 can effectively alter the charge carrier density on PPy. The rGO/PPy nanocomposite's performance of sensing H_2O_2 enhancement is due to the large surface area and strong interactions between the rGO sheet and PPy NPs. Also, the signal transduction is improved because of the enhancement of the p-type behavior. It is observed that the p-type behavior of PPy increases with H_2O_2 concentration.

3.4 Summary

In this chapter, SiO_2 trench-based rGO/PPy nanocomposite -based H_2O_2 sensors have been fabricated using lithography technique. The material properties were characterized using Raman spectroscopy, XRD, FTIR and FESEM images. The sensing performance of H_2O_2 was initially analyzed in cyclic voltammetry to validate the sensing occurence. Then, the sensing performance was analyzed in the fabricated device using 4200 parametric analyser. By characterizing the electrical signal response of solutions including AA, UA, glucose, galactose, sucrose, and urea, the high selectivity of H_2O_2 is also confirmed. The sensor was excellently stable for up to 21 days. Our results are more promising in the case of sensitivity, response time and LOD than those reported earlier with the additional benifit of having a trench structure for liquid storage.

Chapter 4

NON-ENZYMATIC GLUCOSE DETECTION USING GO/Ag NANOCOMPOSITE

4.1 Introduction

This chapter demonstrates the application of graphene oxide-silver (GO/Ag) nanocomposite to develop a non-enzymatic high-performance glucose-sensing field-effect transistor (FET). Overconsumption of glucose in the body, on the other hand, leads to weight gain and health issues. Excess glucose levels in the body cause some diseases, including diabetes mellitus and its complications [33]. The fact that more young individuals are developing diabetes is a cause for concern [34]. Insufficient insulin secretion, inability to make insulin, or inability to metabolize the insulin produced limits diabetes sufferers, leading to the body's failure to manage blood sugar and metabolic issues [115, 116]. Under fasting conditions, healthy persons have a blood glucose level of roughly 3.9 mM-5.5 mM, whereas adults with diabetes have a blood glucose level of around 4.4 mM-7.2 mM. This implies

that persons who have diabetes have higher blood glucose levels than those who do not [34]. As a result, an easy way to reliably and accurately detect glucose is required for clinical diagnostics and patient monitoring.

Clark and Lyons first developed an enzyme-based electrode based on the biocatalytic feature of glucose oxidase, or GOx [117]. This was improved even further, resulting in the development of redox electrodes for clinical diagnosis and diabetes control at the point of use [118, 119]. Despite their effectiveness, enzyme-based glucose sensors face a variety of challenges, including GOx immobilisation on electrodes, long-term stability, heat and chemical stability, handling, and the tendency to readily lose activity after reuse due to washing and drying procedures[120, 121, 122, 123]. Non-enzymatic sensors have thus been developed to address these limitations, as they provide the benefits of low cost, and massive production [124]. Furthermore, because non-enzymatic sensors do not include biological components, they are unaffected by parameters such as lifespan, temperature, humidity, solvent, and other interfering elements. Also, they are more stable than enzymatic sensors [125]. Walther Loeb was the first to investigate the possibility of a non-enzymatic glucose sensor [126]. Since then, non-enzymatic glucose sensor research has sparked a lot of interest, with a variety of technologies and materials being used. Various attempts have recently been made to use electrochemical-based technologies for nonenzymatic glucose detection with quick response and precise readings such as cyclic voltammetry (CV), amperometric measurements, potentiometric measurements, colorimetric determination, FET based sensor, etc [71, 34, 127, 128, 129, 33, 130]. In comparison to previous detection approaches, field-effect transistors (FETs) adopting diverse nanostructures provide a stable and economically practical platform for achieving high current amplification with a sustained and increased signal-to-noise ratio. FET-based

sensors are attracting a lot of attention because of their high sensitivity and ability to monitor bio- and chemical molecules in real time [33, 35].

Additionally, one of the most challenging aspects to detect glucose is choosing a channel material for developing a FET-based sensor. Metal nanoparticles have been employed as a modifier for glucose detection because of their large surface areas and electrocatalytic capabilities. The use of a wide variety of transition metal electro-catalysts, such as Pt, Co, Ni, Cu, Au, W, Ag, and some of their oxides, in the development of non-enzymatic glucose sensors has great interest [131, 132, 133, 70]. Furthermore, by stabilising the metal nanoparticles with a suitable material, their capabilities can be enhanced. For metal nanoparticles, GO offers a chemically and mechanically stable [70, 71, 72]. As a result, we explore the advantages of GO and Ag NPs, as well as their nanohybrids, in order to improve overall sensing performance over that of a previously reported glucose sensor.

The objective of this chapter was to develop hybrid materials with a simple synthetic process while also improving sensing performance. Using GO/Ag nanocomposite SiO_2 trench embedded Field effect transistors, we built a high-performance glucose sensor (FET). Because Ag NPs would operate as a conductive channel sandwiched between GO layers, the GO/Ag nanocomposite are predicted to have increased conductivity and high sensing capabilities. The structure and morphology of the GO/Ag nanocomposite were studied using material characterisation. The strength of the reaction was studied as a function of glucose levels. The sensitivity and limit of detection were also determined, and the results were compared to previously published glucose sensors. The suggested construction includes a SiO_2 trench and a reservoir, eliminating the need for an additional well to hold the analyte liquid.

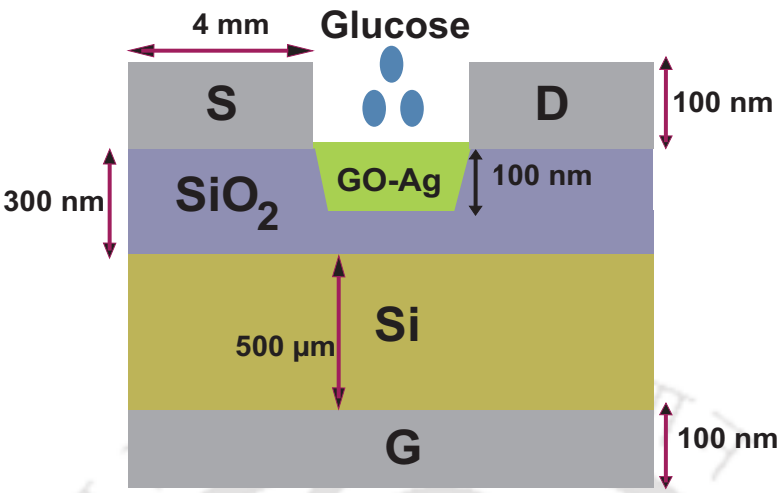

Figure 4.1: The cross-sectional schematic view

4.2 Materials and Method

4.2.1 Preparation of Materials

Silver nitrate ($NaNO_3$), Sodium borohydride $NaBH_4$ were purchased from Sigma Aldrich, India. The modified Hummers method is used to synthesized graphene oxide (GO) [105]. For GO/Ag Nanohybrid, $AgNO_3$ of 0.004 M was slowly mixed in an iced bath under continous stirring for 1 hour [134]. Then $NaBH_4$ of 63 mg was slowly added. For ensuring the silver was reduced entirely, the reaction was kept under stirring overnight [135].

4.2.2 Fabrication of sensing device

The device fabrication process is same as the chapter 2, section 2.3. The GO/Ag nanocomposite was dropcasted as an active channel material for the detection of glucose once the device was fabricated. The dropcasted material was made dry on hotplate at 45° C for 30 minutes. Then we wait for the hotplate to cool down to room temperature. The device was then placed in a desiccator to shield it from

the negative effects of the environment. Figure 4.1 shows the schematic side view of the device.

4.3 Results and Discussions

4.3.1 Material characterisation

Material characterisation using various instruments was carried out to assure the development of chemical interactions between the GO and Ag NPs. The Raman analysis was carried out using a Horiba LabRam HR Evolution Raman spectrophotometer from the United States. A PerkinElmer spectrometer was used to obtain Fourier transform infrared (FTIR) spectra. The surface morphology of the nanocomposite was also imaged using a Field Emission Scanning Electron Microscope (FESEM). The crystallinity of the materials was investigated using X-ray powder diffraction (XRD).

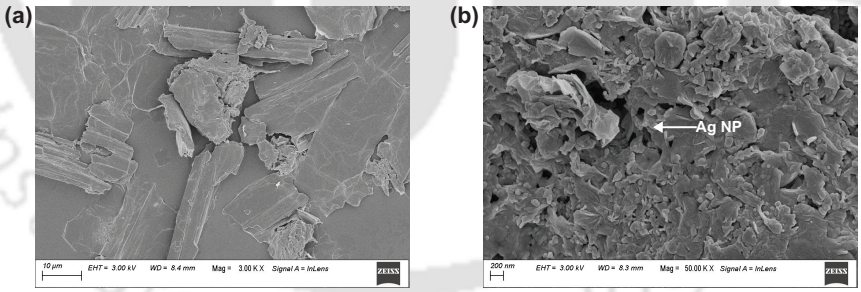

Figure 4.2: FESEM images of (a) GO, (b) GO/Ag nanocomposite

FESEM Analysis

The morphologies of GO, and GO/Ag nanocomposite was analysed using FESEM images shown in Figure 4.2. The interactions of Ag NPs nanoparticles with the GO sheets can be seen in (a) the FESEM picture of GO sheets and (b) the FESEM

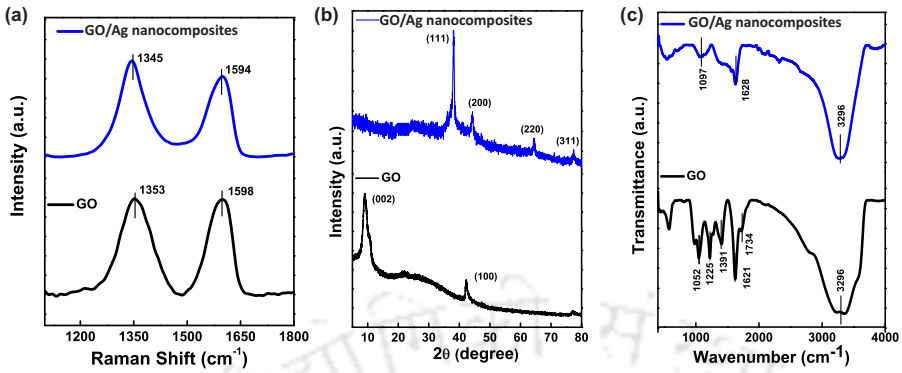

Figure 4.3: (a) Raman spectra of GO, and GO/Ag nanocomposite , (b) XRD pattern of GO, and GO/Ag nanocomposite, (c) FTIR spectra of GO, and GO/Ag nanocomposite

image of GO/Ag nanocomposite material. On the surface area of the GO sheets, the Ag nanoparticles structure was well-organized. The following explanations will assist in realizing the GO/Ag nanocomposite's associated interactions and consistency.

Raman Analysis

The Raman study was carried out to analyse the structure of GO and GO/Ag nanocomposite, as shown in Figure 4.3 (a). The GO Raman spectrum displays two significant bands, correspond to D and G bands, at 1353 cm^{-1} and 1598 cm^{-1}, respectively. The increasing intensity of the D band at 1345 cm^{-1} of Raman spectra for GO/Ag nanocomposite resulted in a shift of both bands to lower wavenumber. [136].

XRD Analysis

XRD was used to examine the crystalline state of the produced GO and GO–AgNP nanohybrid. At room temperature, data for both GO and GO–AgNP samples were

collected from 1 to 80° 2θ. Bragg's law (λ= 2d sinθ) was used to compute the interlayer separation. Figure 4.3 (b) shows the (001) diffraction peak of GO appears at 2θ= 11.1°; according to Bragg's diffraction equations, the d spacing of GO is 0.79 nm. Strong Bragg reflections can be seen in GO–AgNPs patterns at 38.3°, 44.2°, 64.5°, and 77.3°, which correspond to the (111), (200), (220), and (311) crystal planes of AgNPs' face-centred cubic crystal structure, respectively [136]. The development of AgNPs on the GO surface is confirmed by our observations. Furthermore, the absence of the GO diffraction peak after the attachment of AgNPs to its surface shows that GO–AgNP sheets have exfoliated.

FTIR Analysis

Figure 4.3 (c) represents the FTIR spectra of GO, GO/Ag nanocomposite. The GO spectrum has several bands associated with the vibrational modes of various oxygen-containing functional groups. At 3800–3000 cm^{-1}, the stretching vibrations of structural OH groups and physisorbed water molecules can be seen. The $C = O$ carbonyl stretching of COOH groups at the edges of the GO sheets is represented by the band at 1734 cm^{-1}. The deformation vibration of water molecules is represented by the band at 1621 cm^{-1}. The bending of tertiary $C - OH$ groups and the vibration of C–O of epoxide groups ($C - O - C$) produce the peaks at 1362 cm^{-1} and 1052 cm^{-1}, respectively. The $C - O - C$ stretching peak at 1225 cm^{-1} is referred to as $C - O - C$ stretching [136]. For GO/Ag nanocomposite, the carbonyl (between 1900 and 1600 cm^{-1}) and hydroxyl bands (3400-3200 cm^{-1}) bands are weakening.

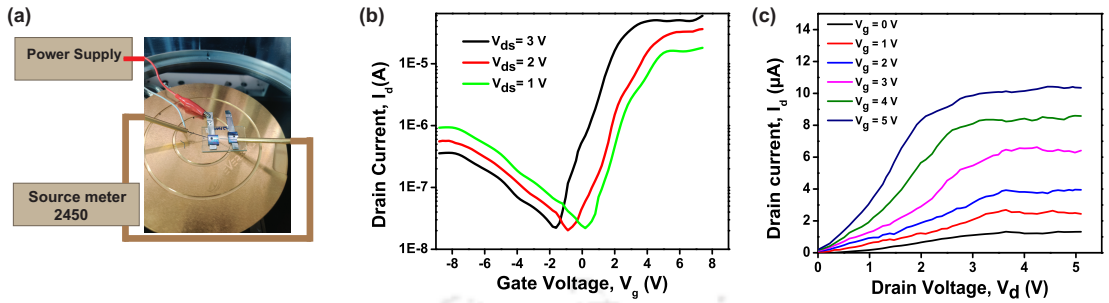

Figure 4.4: (a) Device measurement set-up, (b) Transfer characteristic of GO/Ag nanocomposite FET device, (c) Output characteristic of GO/Ag nanocomposite FET device

4.3.2 Device Characterization Setup and analysis

DC probe station, 2450 source meter, and power supply were used to test the fabricated devices. Figure 4.4 (a) depicts the schematic arrangement. The device was mounted on aluminium foil and connected to a power supply that functioned as a back gate probe for applying the gate voltage. The source and drain contact pads were probed with the two Tungsten probes from the 2450 source meter device. The power supply and source meter supplied the required gate and drain voltages via the probe station and correspondingly measured the device current.

The transfer characteristics of the fabricated devices are shown in Figure 4.4 (b). The graph clearly shows a significant gate dependency of drain current. The gate voltage was set to 3 V in the following experiments so that even minor changes in the channel layer result in a significant rise in drain current. We further investigated the electrical properties of the GO/Ag nanocomposite's conductive channels by measuring the output current-voltage (I_{DS}-V_{DS}) characteristics at various gate biases. Figure 4.4 (c) depicts the usual properties of n-channel transistors, where I_{DS} rises as gate bias rises. It indicates that the device's current was caused by electron transport, and that the electron carrier density at the surface of GO/Ag nanocomposite controls the modulation of I_{DS}.

4.3.3 Electrical Characteristics of FET Based Glucose Sensors

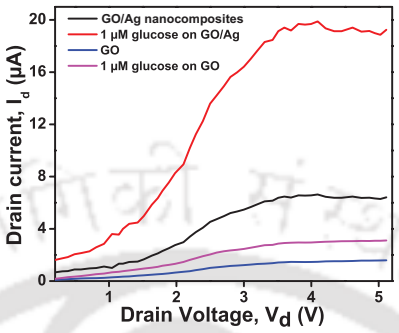

Figure 4.5: 1 μM glucose sensing ouput characteristic of GO and GO/Ag nanocomposite FET device

Figure 4.5 shows the glucose sensing current enhancement when GO/Ag nanocomposites was introduced over GO alone.

The non-enzymatic glucose detection as FET features is investigated using GO/Ag nanocomposite as a conductive channel material. At Vg = 3, we investigated the output characteristics of 1 μM glucose sensing employing individual GO and GO/Ag nanocomposite in our built device. When GO alone acts as a channel, the glucose sensing current is very small, and it cannot be termed a sensing signal since the signal to noise ratio is much less than 3 [111, 15]. When GO/Ag nanocomposite are used as channel material, however, the current is increased. As a result, employing our fabricated back gated device with GO/Ag nanocomposite as sensing material, the detection limit could be enhanced. Because the GO/Ag nanocomposite have greater glucose sensing current than GO alone, it was chosen as the active channel material for the fabricated device. For analysing various glucose concentrations as sensor output characteristics, the gate voltage (Vg) was fixed at 3.0 V (Figure 4.6 (a)). When the glucose concentration rises, the output current rises significantly. The responses of sensing current with constant gate and

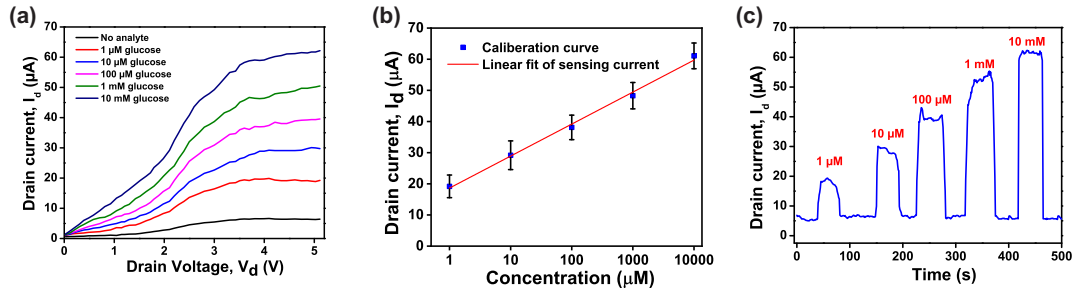

Figure 4.6: (a) Glucose sensing output characteristics of GO/Ag nanocomposite FET device, (b) Calibration curve, (c) Transient response of glucose sensing ranging from 1μM to 10 mM at Vg = 3 V and Vd = 4.5 V

drain voltage were recorded and a calibration curve was obtained in (Figure 4.6 (b)). With R^2=0.99082 at Vg = 3 V and Vd = 4.5 V, the measured calibration for sensing current vs different glucose concentrations (ranging from 1μM to 10 mM) showed exponentially linear nature. This indicates that current has a decent exponentially linear dependence in the specified range. Because healthy people have blood glucose levels of around 3.9 mM-5.5 mM and the current study presents that our device is very sensitive from 1 μM to 10 mM range, it is a promising device that can be used for early stage diabetes detection.

4.3.4 Transient Response of various glucose concentration

The real-time response of our fabricated n-type FET sensor at Vg = 3 and Vd = 4.5 V was characterised by varied glucose concentrations. The changes in drain current (I_{SD}) are measured in relation to the variation in glucose concentration. The drain current (I_{SD}) increases steadily as the concentration of glucose increases due to the formation of n-type charge carriers at the GO/Ag nanocomposite composite surface (Figure 4.6 (c)). The signal to noise ratio of sensing current should be more than or equal to 3 [111, 15]. The SiO_2 trench FET device using GO/Ag nanocomposite exhibits sensitive responses to 1 μM glucose with value of 3.5

signal to noise ratio. As a result, detection limit of our glucose sensor is 1 μM.

4.3.5 Selectivity and sensitivity

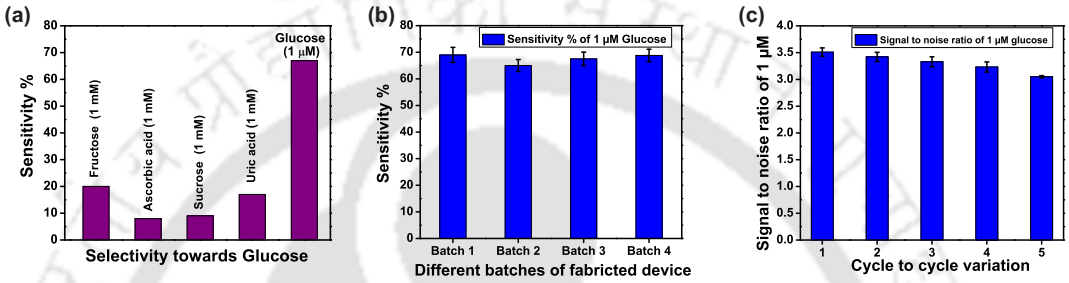

Figure 4.7: (a) Selectivity towards glucose, (b)) Sensitivity % for 1 μM glucose of different batches of fabricated devices, (c) Signal to noise ratio for 1 μM glucose of single fabricated device in several cycles,

The suggested device's specificity was thoroughly investigated. Due to their comparable nature, the molecules Ascorbic acid, fructose, Sucrose, and Uric acid were examined. In Figure 4.7 (a), the sensor's reaction was approximated towards them and compared to glucose.

The sensitivity % was calculated using the following equation from the normalised change in current.

$$\frac{\Delta I_{SD}}{I_0} = \frac{(I_{SD} - I_0)}{I_0} \times 100 \tag{4.1}$$

where I_0 is the base current and I_{SD} is the measured current of individual concentration of glucose. Table 4.1 describes the the level of sensitivity achieved by the glucose against other biological fluids. Sensitivity analysis shows that the present sensor is extremely selective for Glucose.

Table 4.1: Cross sensitivity of glucose with other biological fluids

Fluid	Molarity	Sensitivity %
Fructose	1 mM	20
Ascorbic acid (AA)	1 mM	8
Sucrose	1 mM	9
Uric acid (UA)	1 mM	17
Glucose	1 μM	67

4.3.6 Repeatability

Every biosensing device must have precise repeatability across several fabrications. To assess the repeatability of device performance, a sensitivity of 1 μM at Vg = 3 V and Vd = 4.5 V is performed across various batches of manufactured devices with the same specification. The measured sensitivity is shown in Figure 4.7 (b). Batch-to-batch variation is less than ± 2 % of the mean reading.

We used a single device to investigate the sensor's reusability. From the sixth cycle onwards, the 1 μM of glucose sensing is observed to be degraded, as illustrated in Figure 4.7 (c). This could be owing to the channel layer's many washing. For 1 μM glucose, the signal to noise ratio is greater than 3 until the sixth measurement, with no notable variation. However, by the seventh measurement, the signal to noise ratio has dropped below 3, and hence the sensing of 1 μM glucose cannot be assured [111, 15].

4.3.7 Stability

As demonstrated in Table 4.2, the response time obtained for our SiO_2 trench FET-type sensor, < 5 s, is comparable to other Glucose sensors. After multiple testing, our sensor shows good reproducibility with no change in reaction. Stability is another important feature of a biosensor. Over time, the device's performance

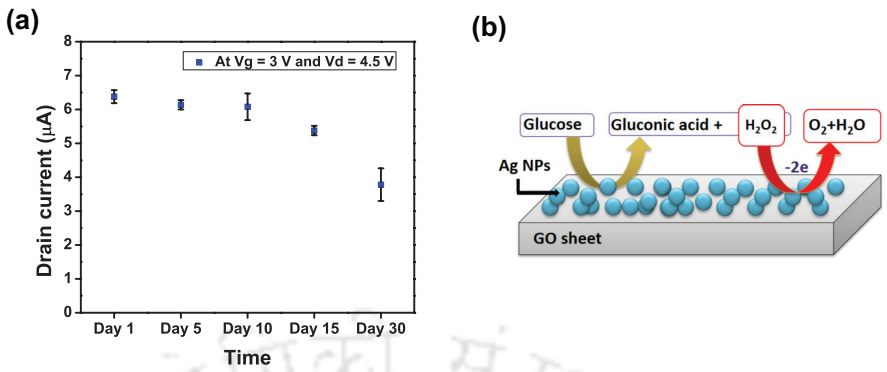

Figure 4.8: Device self stability analysis in several days.

should not deteriorate. As shown in Figure 4.8 (a), some of the devices fabricated during this experiments were stored in a normal laboratory environment (room temperature) and their performance was measured at various time intervals over a significant period of time to determine the channel layer's stability. The devices were quite stable upto 30 days without significant variation.

Table 4.2: Performance comparison of the Various glucose Sensors

Material	**Configuration**	**Response Time**	**Detection limit**	**Year**	**Ref**
Fe2O3-ZnO NRs	Nonenzymatic FET	$<$ 10 s	70 μM	2017	[33]
NiO QDs-ZnO NRs/ Polyimide	Nonenzymatic FET	$<$ 10 s	26 μM	2017	[35]
Ni60Nb40 Nanoglass	Cyclic voltammetry	$<$ 5 s	100 nM	2020	[137]
CuO Nanowire	Extended-Gate FET	$<$ 5 s	1 pM	2020	[138]
NiCo2O4 nanobelt	Cyclic voltammetry	4 s	0.9 μM	2020	[32]
Nafion/GOx/rGO/ ZnONRs/Au/PE	Cyclic voltammetry	$<$ 5 s	1 pM	2021	[139]
GO/Ag nanocomposite	**SiO_2 trench FET with back gate**	**$<$ 5 s**	**1 μM**	**2022**	**This work**

4.3.8 Sensing Mechanism

The sensing layer of the proposed sensor is made up of a combination of GO and Ag NPs. Both GO and Ag NPs have a high level of oxygen interaction and catalytic activity. The glucose that was added during the sensing experiments decomposes in the following way:

$$\text{Glucose} \rightarrow \text{Gluconic acid} + H_2O_2$$

$$H_2O_2 \rightarrow 2H_2O + O_2$$

Glucose is transform to D-glucono-1,5-lactone (also known as gluconic acid) and H_2O_2 in the first step. Secondly, oxygen is released by decomposing H_2O_2 [140]. The oxygen atoms generated are adsorbed onto the GO/Ag nanocomposite composite. Sensing glucose with GO/Ag nanocomposite resulted in increased electrical signal changes compared to the other studies in Table 3.2. This is because both GO and Ag NPs have strong interactions with oxygen atoms, and Ag nanoparticles on GO have a higher surface area electrocatalytic properties [141]. As a result, the composite's adsorption is improved, and the current increase is greater. The GO/Ag nanocomposite sensing mechanism of glucose resulting in the characteristics given in Figure 4.8 (b).

4.4 Summary

In this chapter, using a SiO_2 trench FET based sensor, the application of a non-enzymatic glucose sensor based on the decorating of silver nanoparticles on graphene oxide (GO) was studied. Raman spectroscopy, XRD, FTIR, and FE-SEM images were used to characterise the material properties. This fabricated

device has high sensitivity, stability upto 30 days without significant difference. It also has fewer than 5 s response time, and a detection limit of 1 μM glucose with an appropriate signal to noise ratio. The high selectivity of glucose is also confirmed by analysing the electrical signal response of solutions containing AA, UA, fructose, and sucrose. Our study results are more promising than those previously reported, with the added benefit of a trench structure for liquid storage, which could also be used for sensing purposes.

Chapter 5

LACTATE FUNCTIONALISED GO/Ag NANOCOMPOSITE FOR LABEL FREE LACTATE DEHYDROGENASE DETECTION

5.1 Introduction

This chapter demonstrates a novel electrochemical detection method of lactate dehydrogenase (LDH) in SiO_2 trench embedded device-based. LDH is an enzyme that is found in nearly all cell types, which facilitates the glycolytic processes by reversibly catalyzing the conversion of pyruvate into lactate, and vice versa. High levels of LDH are often considered to be an indication of tissue damage. In the case of cancer, research evidence suggests that LDH is often found to be elevated, which is attributed to the accelerated glycolysis (also known as the Warburg effect) in malignant cells [39]. The aberrant expression and activation of LDH are found to be closely associated with almost all cancer subtypes. Therefore, it can be

considered as a predominant biomarker of cancer progression and dissemination.

LDH measurement methods that are simple and easy to use are highly relevant and useful in diagnostic tests. Colorimetric detection of formazan dye employing nicotinamide adenine dinucleotide (NAD) as a coenzyme and lactic acid as a substrate is one of the most extensively used techniques for measuring LDH levels [38]. The test is sensitive, but it requires expensive equipment, such as a plate reader, many sample handling procedures, and experienced workers to execute, making it inappropriate for resource-constrained environments. Furthermore, because the reagents have poor thermal and photostability, they must be delivered and maintained in the dark at low temperatures to minimise degradation, increasing the assay's cost. Another group used a nonporous, oxygen impermeable, reversibly gelling polysaccharide material based on pullulan to develop a paper-based point-of-care (POC) colorimetric biosensor for the detection of lactate dehydrogenase in serum. The pullulan, as well as all of the essential assay chemicals were printed onto paper surfaces [142]. Despite paper-based sensors have a lot of potential, they have some drawbacks, such as accuracy and sensitivity.

Also, there are also few existing commercial kits of LDH sensor. The Amplite® Lactate Dehydrogenase Assay Kit uses an absorption-based approach to detect L-lactate dehydrogenase (L-LDH) in biological samples such serum, plasma, and urine, as well as cell culture samples. It is capable to detect as low as 3 mU/mL of L-lactate dehydrogenase in a 100 μL reaction volume. The other team developed an LDH assay kit that uses coenzyme I as a hydrogen carrier. LDH catalyses the conversion of lactic acid to pyruvate. Pyruvate dinitrophenylhydrazone was formed when pyruvate reacted with 2, 4-dinitrophenylhydrazine in an alkaline solution, and the colour depth is proportional to the pyruvate content. LDH GloTM Cytotoxicity Assay is another kit that uses bioluminescent plate-based

assay to detect LDH release into the culture medium upon plasma membrane damage. There is also Lactate Dehydrogenase (LDH) Assay Kit (Colorimetric) ab102526 that quantifies LDH activity in a variety of samples such as serum or plasma, tissue, cells, and culture medium. As a result, detecting LDH using this enzymatic technique will be highly successful. A device-based electrochemical detection technique that is cost-effective, selective, and reliable is required for the measurement of LDH concentration. Herein, for the first time, a device has been fabricated and functionalized to detect the occurrence of a chemical reaction in real time by employing its IV characteristics for LDH detection.

One of the most difficult aspects for biosensor is choosing a channel material for sensing a certain analyte. Nanoparticles, semiconductor heterostructures, and hybrid materials are examples of channel materials. Because of its enormous surface area, polar functionalization, low cost and easy workability, graphene oxide (GO) is one of the viable channel material among them [143]. Silver nanoparticles (Ag NPs) are another well-known materials due to their excellent conductivity, chemical stability, and electrocatalytic characteristics [144, 145]. In addition, Ag NPs in biosensors permit more efficient electron transport than other nanoparticles, have a higher sensitivity than other nanoparticles, and are successfully conjugated to biomolecules. As a result, we investigate the benefits of GO and Ag NPs and select nanohybrids that allow Ag NPs to bind with lactate and conduct an enzymatic reaction on the device, resulting in improved overall sensing performance.

5.2 Exerimental Setup

The flow of the fabrication process device is same as chapter 2, section 2.3. The GO/Ag nanohybrid was drop cast as an active channel material for the detection

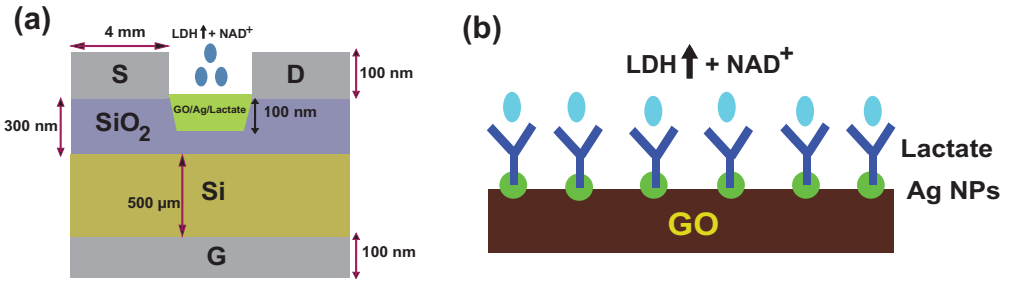

Figure 5.1: (a) Schematic device structure (c) Schematic binding

of LDH once the device was fabricated. The channel material was dried for 30 minutes at 45 °C, and then gradually cooled to room temperature. In addition, for the enzymatic experiment, 0.05 mM lactate is dropcasted. Following that, the lactate-bound device was vacuum dried to obtain the lactate functionalized GO/Ag nanocomposite channel material. Figure 5.1 (a) depicts the schematic side view of the device.

5.2.1 Functionalization

To conduct the enzymatic assay and to achieve detection of LDH, the lactate was bound electrostatically to the Ag nanoparticles which were thoroughly organized on the surface of GO sheets as shown in Figure 5.1 (b). Lactate presence helps to conduct assay with the addition of LDH and NAD^+. Because Lactate was bound to the nanoparticles alone, the conjugation process between them could only take place at the surface of GO/Ag nanoparticles in the presence of both LDH and NAD^+. As a result, the effect of additional oxidation-reduction reactions in the analyte on the electrochemical device's output characteristic was completely eliminated. The detection of LDH was particularly specific because the device properties changed according to the electrochemical processes on the surface of the nanoparticles.

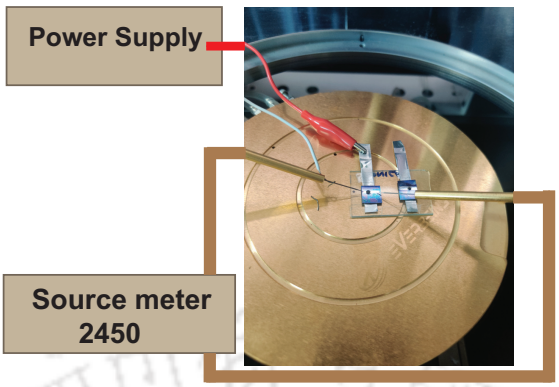

Figure 5.2: Device measurement set-up

5.2.2 Measurement setup

All the measurements were taken using 2450 source metre and power supply, and probing was done using a DC probe station. The contact was probed by the terminals of the probe station and connected to the SMU's of the parameter analyzer. Figure 5.2 depicts the schematic arrangement. The device was placed on foil and linked to a power source that served as a back gate probe for applying the gate voltage. The two Tungsten probes from the 2450 source metre device were used to probe the source and drain contact pads. The probe station received the needed gate and drain voltages from the power supply and source metre.

5.3 RESULTS AND DISCUSSION

5.3.1 KINETIC CHARACTERIZATION OF LDH

The lactate dehydrogenase (LDH) was obtained from Sigma-Aldrich (Roche), which catalyzes the conversion of Pyruvate and NADH into lactate and NAD^+, and vice versa. The characteristic absorbance of the NADH at 340 nm was used to monitor the rate of the enzyme-catalyzed reaction [146]. The reactions were

performed using 20 mM Tris-Cl, pH 8.0. The reaction was initiated upon the addition of 550 U/ml (or 1000 μg/ml) of the enzyme to a total reaction volume of 1 ml (final concentration of the enzyme was 5.5 U/ml (10 μg/ml)), following which the absorbance was measured at 340 nm using Cary 60 UV-Visible spectroscopy (Agilent technologies, Santa Clara, California, US). Furthermore, the concentration of NADH is obtained using the formula:

$$\text{Concentration of NADH} = \frac{\text{absorbance}}{6200 \times 1}\text{M} \tag{5.1}$$

Where, molar extinction coefficient of NADH = 6220 M^{-1} cm^{-1}; pathlength of cuvette = 1 cm. The enzyme's affinity for lactate and its kinetics against lactate was determined by varying its (sodium lactate) concentration from 5 to 350 mM while maintaining the concentration of NAD^+ at 10 mM. Similarly, the enzyme's affinity for NAD^+ and its kinetics against NAD^+ was determined by varying its concentrations from 0.5 to 20 mM, while keeping the concentration of the lactate constant at 250 mM. The specific activity (mU/μg) was plotted against varying the substrate concentrations of lactate and NAD^+ according to the formula:

$$\text{specific activity} = \frac{\text{NADH initial} - \text{NADH final(nmol)}}{\text{time (min)} \times \text{Amount of enzyme}(\mu\text{g})} \tag{5.2}$$

The substrate concentration at half the maximum velocity (Km) and the maximum velocity (Vmax) of LDH was then determined using the GraphPad Prism software. To assess the effect of temperature on LDH activity, the LDH activity assay was set up at temperatures ranging from 4° C to 55° C, keeping the substrate and enzyme concentration constant (150 mM of sodium lactate, 5 mM NAD^+ and 5 μg/ml of LDH, respectively). The activity of the enzyme at varying temperatures was plotted using the GraphPad Prism software. Similarly, the

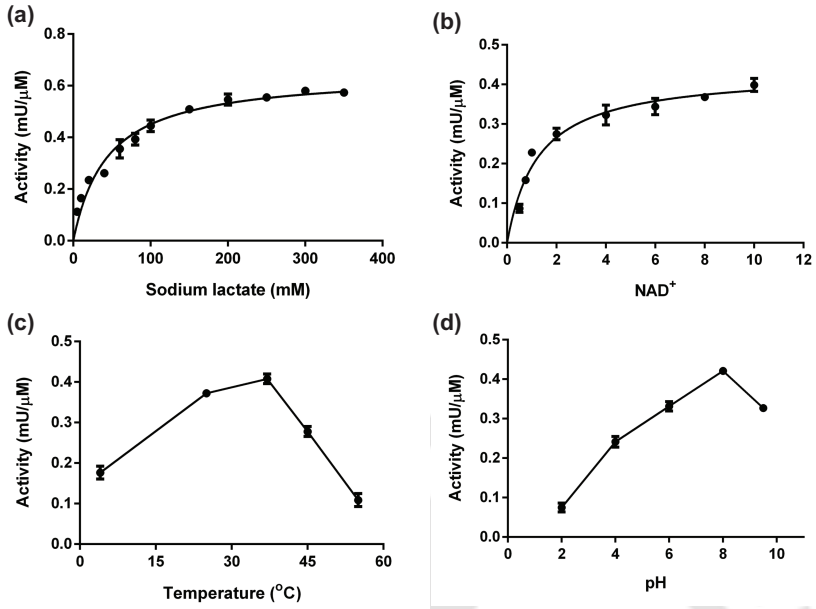

Figure 5.3: Kinetic parameters of LDH. The plot of activity vs increasing concentration of (a) sodium lactate and (b) NAD^+. The effect of (c) temperature and (d) pH on LDH activity.

effect of pH was monitored using three different buffers: KCl-HCl buffers of pH 2, citrate buffer for pH 4 and 6, whereas 20mM Tris-Cl for pH 8 and 9.5, respectively. Herein, the lactate and NAD^+ were dissolved in the corresponding buffers to maintain the desired pH, following which the reaction was carried out. Finally, the GraphPad Prism software was used to access the graph for the activity vs pH of the enzyme.

From the kinetic profile of the enzyme, it is inferred that the LDH activity against sodium lactate and NAD^+ follows Michaelis-Menten kinetics. The kinetic parameters Km, Vmax and Kcat were determined from the plot of activity vs. substrate concentration using GraphPad Prism software (Figure 5.3). Following this, the enzyme efficiency (which is the ratio of Kcat to Km) was calculated, depicted in Table 5.1. The maximum velocity (Vmax) of the reaction was found to be 0.6497 mU/μg for sodium lactate and 0.4325 mU/μg for NAD^+. Furthermore,

Table 5.1: Kinetic parameters of LDH against sodium lactate and NAD^+

LDH	K_m (mM)	V_{max} (mU/μg)	K_{cat} (min^{-1})	K_{cat}/K_m ($m^{-1}min^{-1}$)
Sodium lactate	44.25 ±0.0157*	0.6497 ± 0.05*	3.611	8.16 ×10 5
NAD^+	1.123 ±0.0135*	0.4325 ±0.03*	94.67	8.43 ×10 4

*The assays were conducted at 25° C and the data are presented as mean ± SEM, with n=3 independent determinations for each sample. *The significant difference is at p<0.0001 for sodium lactate and p=0.0009 for* NAD^+

the kinetic profile of the LDH at various temperatures and pH was carried out using a fixed concentration of the substrate, co-factor and enzyme (150 mM of sodium lactate, 5 mM NAD^+ and 10 μg/ml of LDH, respectively). The kinetic profile of LDH at temperatures ranging from 4 to 55° C depicted an increase in enzyme activity with the increase in temperature, with maximum activity at 37° C and above which the activity decreases. This is attributed to the degradation of the enzyme at higher temperatures. Similarly, a graph depicting the activity vs pH showed maximum activity at pH 8 (Figure 5.3), thereby suggesting that the enzyme retains its functional characteristics similar to that in the human physiological conditions.

5.3.2 Detection of LDH

To validate the sensing ability, electrochemical detection of LDH with GO, GO/Ag NPs composites was performed initially. For sensing LDH, the signal to noise ratio of GO alone is 1.1, which is not acceptable as shown in Figure 5.4 (a). However, the signal to noise ratio for GO/Ag NPs composites LDH sensing is 3, which can be considered. Because the sensing current of LDH is larger than that of GO, hence, the GO/Ag NPs is chosen as the active channel material for the fabricated device.

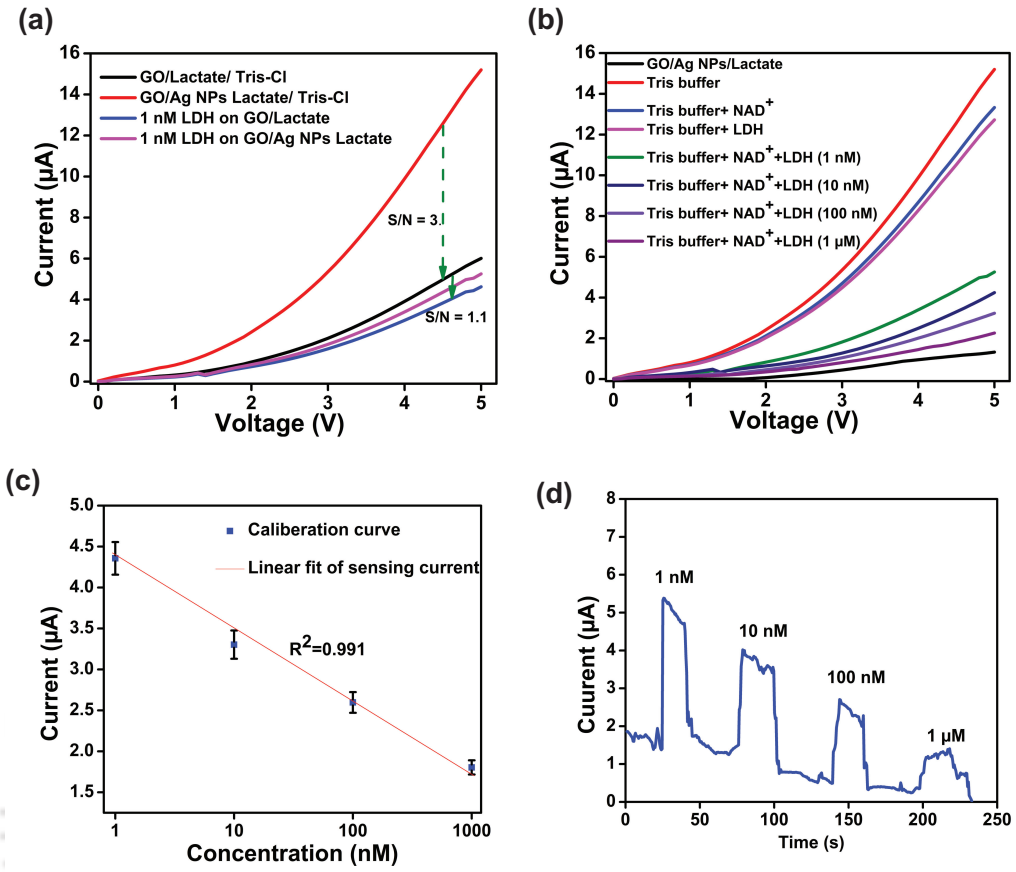

Figure 5.4: (a) LDH sensing with GO and GO/Ag NPs individually, (b) IV Characteristics of LDH sensing, (c) Calibration curve, (d) Transient response of different concentration LDH sensing.

The I-V characteristics of the device was measured under analytes being applied. Initially, only Tris-Cl was applied, followed by Tris-Cl with NAD^+ only, Tris-Cl with LDH only, and finally, Tris-Cl with different concentrations of LDH and constant concentration of NAD^+. Obtained I-V plots are shown in Figure 5.4 (b). It can be observed from the plot that the response due to Tris-Cl with different concentrations of LDH and NAD^+ combined is much higher than that of Tris-Cl with NAD^+, and Tris-Cl with LDH individually. This is because in presence of both LDH and NAD^+, conjugation reaction between them takes place on the channel where Lactate is present. Since this reaction takes place on the surface

of the channel, the occurrence of this reaction gets reflected on the device characteristics. As visible from the I-V characteristics of the device, the current flowing through the channel decreases by a significant amount in different concentrations of LDH. Subsequently, Figure 5.4 (d) shows the real-time measurement of current at a fixed voltage of 4.5 V. The sudden peaks depict a sudden decrease of current due to the presence of an analyte on the channel. The current reaches a peak, then slowly reduces to somewhere nearby its original value. So, from this plot, we can know the time for which the channel undergoes the conjugation reaction.

5.3.3 Temperature dependence real-time analysis

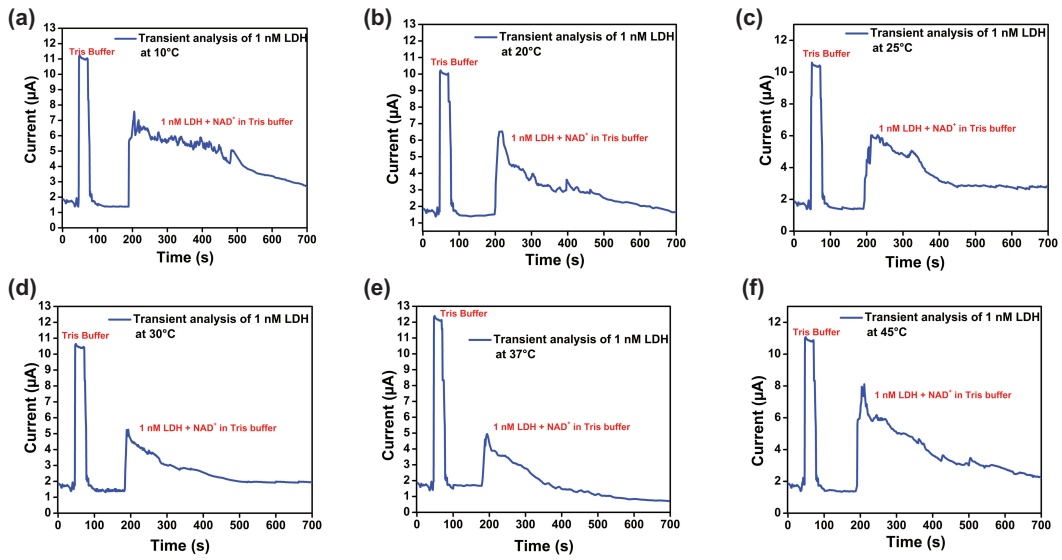

Figure 5.5: Temperature dependence real time analysis at (a) 10° C, (a) 20° C, (c) 25° C, (d) 30° C, (e) 37° C, (f) 45° C

After successful detection of LDH, the device was tested for temperature dependence to see if the device exhibits the property of detection at different temperatures (Figure 5.5). The Tris-Cl was first applied on the channel followed by the LDH + NAD^+ at fixed gate bias. The device was kept at different tempera-

tures 10° C, 20° C, 25° C, 30° C, 37° C, and 45° C for each device measurement. The maximum changes occurred at 37° C, therefore, the optimum temperature of reaction in the device is 37° C. Figure 5.5 shows the result of the temperature dependence of 1 nM LDH detection. The current changes for sensing 1 nM LDH at 37° C has more than the device whose kept at other temperatures. Since the sample is made in Tris-Cl, the Tris-Cl current is taken as base current.

5.4 FET based Cancer cell detection

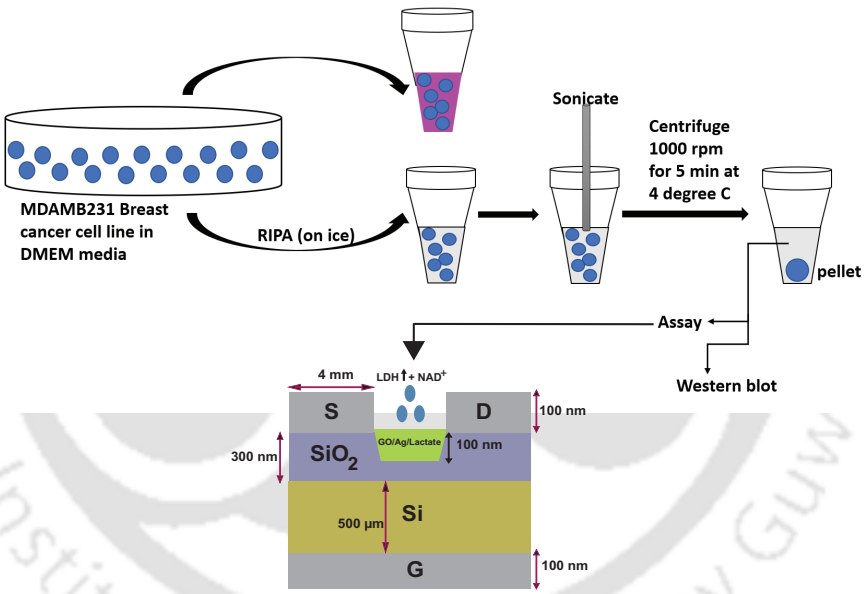

Figure 5.6: Process step of LDH isolation from cancer cell line

Figure 5.6 shows the process step of LDH isolation from cancer cell line. The isolated LDH are used to detect in our fabricated FET device. Research evidences suggests that the accumulation and production of ROS contributes to the conversion of normal cells to cancer cells by mediating genomic instability, oncogenic growth, ECM independency and increased motility. Early identification of breast cancer is essential since it is linked to a greater number of treatment options, a

higher chance of survival, and a better quality of life. While there is no surefire way to prevent breast cancer, early detection gives an opportunity at a successful treatment. Therefore, a novel SiO_2 trench embedded Field effect transistor detection method of cell line secreted LDH (breast cancer cell line, MDA-MB-231) has been described in this chapter too. EGF treated cells were supposedly taken as a positive control, on account of its ability to induce EMT, which in turn are known to induce the expression of LDH.

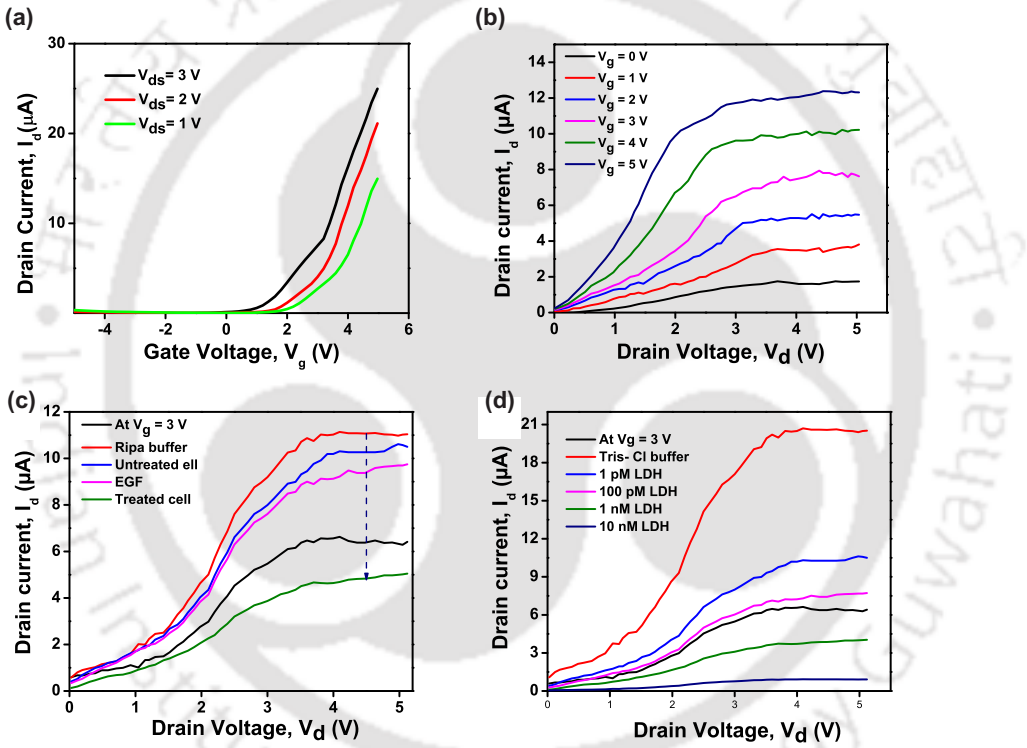

Figure 5.7: (a) Transfer characteristics, (b) Output characteristics, (c) Cell's LDH sensing output characteristics, and (d) Known concentration LDH sensing output characteristics

Before sensing, the device measured transfer characteristics and output characteristics as shown in Figure 5.7 (a-b). In the next studies, the gate voltage was adjusted at 3 V such that even slight changes in the channel layer result in a large increase in drain current. The device's output characteristics were tested with a

variety of analytes. Initially, only RIPA buffer was used, followed by untreated cells, EGF, and eventually, LDH with constant NAD^+ treated cells. Figure 5.7 (c) shows the $I_D - V_D$ plots that were obtained. The reaction owing to LDH (treated cell) and NAD^+ is substantially lower than that due to untreated or EGF with constant NAD^+, as seen in the plot. This is due to the fact that when both LDH and NAD^+ are present, the conjugation reaction between them occurs on the channel where Lactate is present. Because this reaction takes place on the channel's surface, its occurrence is reflected in the device's characteristics. Current flowing through the channel clearly decreases by a large amount in the presence of both LDH and NAD^+, as evidenced by the device's output characteristics. When no gate voltage is supplied, the signal to noise ratio for 1 nM LDH was 3. However, when a gate terminal is biassed at 3 V, the current is increased, and the signal to noise ratio of 3 was achieved by the 100 pM of LDH as shown in Figure 5.7 (d). As a result, our fabricated back gated device improves the detection limit.

5.4.1 Reproducibility, stability, and transient analysis

The drain current is then measured in real time of cell' LDH at a fixed gate voltage of 3 V and a drain voltage of 4.5 V in Figure 5.8 (b). The abrupt peaks represent a drop in output current caused by the presence of an anlayte on the channel. When both treated cell's LDH and NAD^+ are present on the channel, as can be observed, current drops significantly.

Precision repeatability over several fabrications is a must for every biosensing device. I–V characteristics of treated cell's LDH sensing are undertaken across several batches of produced devices with the same specification to assess the repeatability of device performance. The measured sensitivity % of cell's LDH for each device at fixed voltage is shown in Figure 5.8 (d). Batch to batch variation

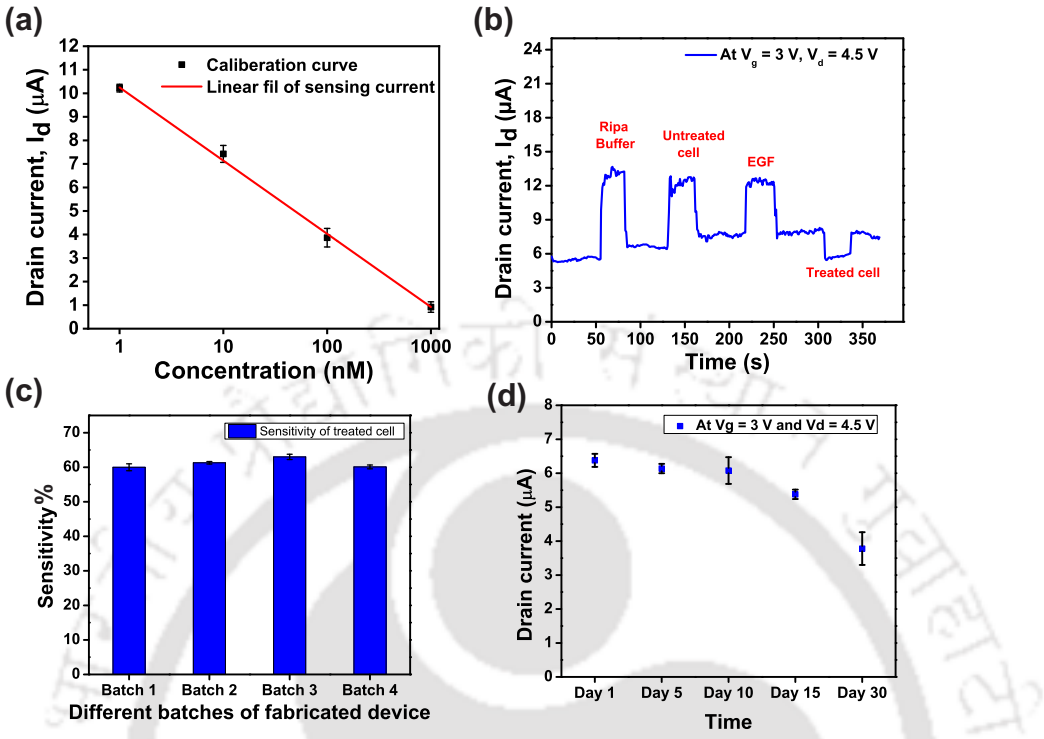

Figure 5.8: (a) Calibration curve of known concentration of LDH sensing current, (b) Transient analysis of cell's LDH, (c)Reproducibility of cell's LDH sensing, and (d) Stability of the Lactate conjugated GO/Ag NPs channel material devices.

is within ±2 % of the mean reading. To check the stability of the channel layer, some of the devices fabricated during this investigation were stored at 4°C and device performance was measured at various time intervals over a lengthy period of time. The output characteristics of device were measured after 1, 5, 10, 15, and 30 days, as shown in Figure 5.8 (d), and they were shown to be highly stable.

5.5 Summary

This chapter describes a GO/Ag nanoparticle – Lactate composite channel-based biosensor for detecting lactate dehydrogenase in vitro (LDH). A functionalized channel layer consisting of a nanoconjugate of GO/Ag nanoparticles and Lactate

was functionalized in a Si-based 20 μm channel length SiO_2 trench. When the conjugation reaction between LDH and NAD^+ occurs in the presence of Lactate on the device's channel, the device's current changes in real-time, confirming the detection of Lactate dehydrogenase (LDH). For the first time, FET-based detection of LDH employing lactate has been described. The device output current may easily detect increased LDH concentration. The fabricated device was also tested with a cancer cell line secreted LDH. This experiment yielded a high sensitivity LDH and a Limit of Detection (LOD) of 100 pM. As a result of this discovery, this device can be used for cancer diagnosis and the efficacy of a treatment.

Chapter 6

CONCLUSIONS AND FUTURE DIRECTIONS

6.1 Conclusion

The summary and prospects of the work covered in this thesis are presented in this chapter. This thesis's ultimate goal was to develop and fabricate a SiO_2 trench embedded FET based device for bio-sensing applications. It began with the invention of a device fabrication technique that was suitable for incorporating analyte. The device was first put to the test with KCl as the ionic liquid channel. Following that, a FET device with a functionalized channel layer was developed for the detection of H_2O_2, glucose, and LDH. The device was also put to the test for detecting LDH levels in malignant cells. The following is a summary of the conclusions made from the chapters of this work:

The first chapter provides a basic overview, outlines the thesis's primary aims and scope, and presents a comprehensive literature survey on the topic.

In the second chapter, the fabrication of a 100-nm deep liquid container in SiO_2 employing photolithography and selective etching was shown in this research. A

Profilometer was used to determine the depth of the SiO_2 trench, and the contact angle technique was used to determine the hydrophobicity of the etched surface. The average (Ra) and rms (Rq) roughness of the etched portion's surface are 1.67 and 2.72 nm, respectively. KCl was employed as an ionic liquid channel to analysed FET characteristics. The theoretically computed C_{total} was $1.29 \times 10^{-4} F/m^2$ after adding Debye capacitance. The electrical characteristics of the FET have been measured and depending on the back gate biasing, both n-FET and p-FET characteristics have been obtained. The number of ions determined from electrical properties was remarkably similar to the number of ions in the solution.

Since simple liquid channel FET excluding any other mold or liquid containing intricate architecture, which can further be used for many bio-sensing applications is proposed, SiO_2 trench-based rGO/PPy nanocompoites based H_2O_2 sensors have been fabricated and discussed in the third chapter. The performance of H_2O_2 as a sensor was first investigated using cyclic voltammetry. Raman spectroscopy, XRD, FTIR, and FESEM images were used to analyse the material characteristics. This fabricated device has a high sensitivity, stability, and a rapid response time of 5 seconds, with a detection limit of 10 pM of H_2O_2. The great selectivity of H_2O_2 is further validated by analysing the electrical signal response of solutions containing AA, UA, glucose, galactose, sucrose, and urea. Our findings are more promising than those previously published, with the extra benefit of a trench structure for liquid storage.

Maintaining glucose levels is much important for preventing health issues such as heart disease, diabetes, vision loss, and kidney disease. Therefore, in the fourth chapter, the use of a non-enzymatic glucose sensor based on the decoration of silver nanoparticles on graphene oxide (GO) was explored. Raman spectroscopy, XRD, FTIR, and FESEM images were used to characterise the material properties. With

a detection limit of 1 μM glucose , this developed device offers great sensitivity, stability, and a response time of less than 5 seconds.

In the last phase of the thesis work, a novel device-based electrochemical detection method of LDH has been described. For the first time, a novel concept of combining a conjugation of GO/Ag nanocomposite and Lactate as a channel material is presented. The device detects and quantifies LDH as a chemical successfully and selectively. The device was also successfully tested with an LDH derived from the breast cancer cell line, MDA-MB-231. The device was discovered to be capable of detecting elevated levels of LDH in malignant cells, which is the first step in detecting some types of acute cancer disease. To meet the needs of a deliverable product for marketization, the device can be developed further by keeping the main working principle the same.

6.2 Future Directions

The investigation and development of biosensors to fabricate realistically advanced electronic components and devices have been the main focus of this thesis, which could provide a reasonable option to silicon microfabrication based devices in terms of size and fabrication simplicity. However, there are several future dimensions to this research area that are discussed below.

- As previously indicated, this research is the first to disclose device-based LDH detection. Although the results are promising and superior to most current LDH detection approaches, there is still room for improvement in terms of device size. The device's properties may be tested using channel lengths in the nanometer range.

- The ability to be transformed into a point-of-care device for commercial

usage is the most significant characteristic of a typical biosensing device. If fabricated properly, the device developed in this work is capable of reaching that goal. This aspect of the work's future prospects is perhaps the most important factor to consider in order to achieve a point-of-care device in the near future.

- The fundamental current model for nanocomposites (GO/PPy, GO/Ag, GO/Ag/Lactate) FET may be model further by applying Poisson's equation to construct a model for channel surface potential. To account for carrier transport in the channel, standard quantum confinement models such as the Schrodinger-Poisson (SP) solver model, the Bohm quantum-potential (BQP) model, and the Landauer current expression can be used.
- Optimizing the channel architecture with 2 or more reservoirs may help to increase the sensitivity of the target.

Table 6.1: Complete summary of fabricated devices and their applications

Chapter	Fabricated Devices/ Structures	Measuring Instrument	Application	Channel Material	Results
2	SiO_2 trench embedded FET	4200 Paramter analyzer	Ionic FET	KCl	$C_{ox_{eff}}$ 20 % more than a uniformly thick 300 nm SiO_2, R_a= 1.67 nm and R_a= 2.72 nm, $C_{Total} = 1.29 \times 10^{-4} F/m^2$, Contact angle of KCl= 66.52°
3	SiO_2 trench embedded FET	4200 Paramter	H_2O_2 detection	rGO/PPy	LOD = 10 pM, Response time = < 5s, Stability = Upto 21 days, outstanding reproducibility, and excellent H_2O_2 selectivity
4	SiO_2 trench embedded FET	2450 source meter, power supply	Non-ezymatic Glucose detection	GO/Ag	LOD = 1 μM, Response time = < 5s, Stability = Upto 30 days, outstanding reproducibility, and excellent glucose selectivity
5	SiO_2 trench embedded FET	2450 source meter, power supply	LDH detection	GO/Ag/Lactate	LOD = 100 pM, Response time = < 5s, Stability = Upto 30 days long-term stability, outstanding reproducibility, and can be used for cancer diagnosis and the efficacy of a treatment

Bibliography

[1] Formisano N Estrela P Bhalla N, Jolly P. Introduction to biosensors. *Essays Biochem*, 60(1):1–8, 2016.

[2] Parikha Mehrotra. Biosensors and their applications–a review. *Journal of oral biology and craniofacial research*, 6(2):153–159, 2016.

[3] Saraju P Mohanty and Elias Kougianos. Biosensors: A tutorial review. *Ieee Potentials*, 25(2):35–40, 2006.

[4] Joseph Wang. Dna biosensors based on peptide nucleic acid (pna) recognition layers. a review. *Biosensors and Bioelectronics*, 13(7-8):757–762, 1998.

[5] Jeffrey D Newman and Steven J Setford. Enzymatic biosensors. *Molecular biotechnology*, 32(3):249–268, 2006.

[6] GA Rechnitz. Biochemical electrodes uses tissues slice. *Chem Eng News*, 56:16–21, 1978.

[7] Chen Chen and Junsheng Wang. Optical biosensors: An exhaustive and comprehensive review. *Analyst*, 145(5):1605–1628, 2020.

[8] Yu-Cheng Syu, Wei-En Hsu, and Chih-Ting Lin. Review—field-effect transistor biosensing: Devices and clinical applications. *ECS Journal of Solid State Science and Technology*, 7(7):Q3196–Q3207, 2018.

[9] Piet Bergveld. Development of an ion-sensitive solid-state device for neurophysiological measurements. *IEEE Transactions on Biomedical Engineering*, (1):70–71, 1970.

[10] Jae-Hyuk Ahn, Jee-Yeon Kim, Kyungyong Choi, Dong-Il Moon, Chang-Hoon Kim, Myeong-Lok Seol, Tae Jung Park, Sang Yup Lee, and Yang-Kyu Choi. Nanowire fet biosensors on a bulk silicon substrate. *IEEE Transactions on Electron Devices*, 59(8):2243–2249, 2012. doi: 110.1109/TED.2012.2200105.

[11] Anqi Zhang and Charles M Lieber. Nano-bioelectronics. *Chemical reviews*, 116(1):215–257, 2016.

[12] Vivek Pachauri and Sven Ingebrandt. Biologically sensitive field-effect transistors: from isfets to nanofets. *Essays in biochemistry*, 60(1):81–90, 2016.

[13] Leila Syedmoradi, Maryam Daneshpour, Mehrdad Alvandipour, Frank A Gomez, Hassan Hajghassem, and Kobra Omidfar. Point of care testing: The impact of nanotechnology. *Biosensors and Bioelectronics*, 87:373–387, 2017.

[14] Leila Syedmoradi, Anita Ahmadi, Michael L Norton, and Kobra Omidfar. A review on nanomaterial-based field effect transistor technology for biomarker detection. *Microchimica Acta*, 186(11):1–23, 2019.

[15] Hyeonseok Yoon, Sungrok Ko, and Jyongsik Jang. Field-effect-transistor sensor based on enzyme-functionalized polypyrrole nanotubes for glucose detection. *The Journal of Physical Chemistry B*, 112(32):9992–9997, 2008.

[16] Tetsushi Sekiguchi, Michihiro Nakamura, Mototsugu Kato, Keiko Nishikawa,

Kaku Hokari, Toshiro Sugiyama, and Masahiro Asaka. Immunological helicobacter pylori urease analyzer based on ion-sensitive field effect transistor. *Sensors and Actuators B: Chemical*, 67(3):265–269, 2000.

[17] Shailly Varma. Electrochemical studies on reconstituted horseradish peroxidase modified carbon paste electrodes. *Bioelectrochemistry*, 56(1-2):107–111, 2002.

[18] Xiaojie Duan, Ruixuan Gao, Ping Xie, Tzahi Cohen-Karni, Quan Qing, Hwan Sung Choe, Bozhi Tian, Xiaocheng Jiang, and Charles M Lieber. Intracellular recordings of action potentials by an extracellular nanoscale field-effect transistor. *Nature nanotechnology*, 7(3):174–179, 2012.

[19] Girish S Kulkarni and Zhaohui Zhong. Detection beyond the debye screening length in a high-frequency nanoelectronic biosensor. *Nano letters*, 12(2):719–723, 2012.

[20] Dong-Sun Kim, Jee-Eun Park, Jang-Kyoo Shin, Pan Kyeom Kim, Geunbae Lim, and Shuichi Shoji. An extended gate fet-based biosensor integrated with a si microfluidic channel for detection of protein complexes. *Sensors and Actuators B: Chemical*, 117(2):488–494, 2006. doi: 10.1016/j.snb.2006.01.018.

[21] Chih-Sheng Johnson Hou, Michel Godin, Kristofor Payer, Raj Chakrabarti, and Scott R. Manalis. Integrated microelectronic device for label-free nucleic acid amplification and detection. *Lab Chip*, 7(3):347–354, 2007. doi: 10.1039/B617082J.

[22] Seokheun Choi, Michael Goryll, Lai Yi Mandy Sin, Pak Kin Wong, and Junseok Chae. Microfluidic-based biosensors toward point-of-care detection

of nucleic acids and proteins. *Microfluidics and Nanofluidics*, 10(2):231–247, 2011. doi: 10.1007/s10404-010-0638-8.

[23] Bo Zhang, Marissa Wood, and Hyunae Lee. A silica nanochannel and its applications in sensing and molecular transport. *Analytical chemistry*, 81(13):5541–5548, 2009. doi: 10.1021/ac9009148.

[24] Dario Lombardi and Petra S Dittrich. Advances in microfluidics for drug discovery. *Expert opinion on drug discovery*, 5(11):1081–1094, 2010. doi: 10.1517/17460441.2010.521149.

[25] D. Kwon, J. H. Lee, S. Kim, R. Lee, H. Mo, J. Park, D. H. Kim, and B. Park. Drift-free ph detection with silicon nanowire field-effect transistors. *IEEE Electron Device Letters*, 37(5):652–655, 2016. doi: 10.1109/LED.2016.2542846.

[26] Julia Foreman, Vadim Demidchik, John HF Bothwell, Panagiota Mylona, Henk Miedema, Miguel Angel Torres, Paul Linstead, Silvia Costa, Colin Brownlee, Jonathan DG Jones, et al. Reactive oxygen species produced by nadph oxidase regulate plant cell growth. *Nature*, 422(6930):442–446, 2003.

[27] J David Lambeth. Nox enzymes and the biology of reactive oxygen. *Nature Reviews Immunology*, 4(3):181–189, 2004.

[28] H Ohshima. Tatemichi m, sawa t. *Chemical basis of inflammation-induced carcinogenesis. Arch Biochem Biophys*, 417:3–11, 2003.

[29] Wakako Maruyama, Philippe Dostert, Kazuo Matsubara, and Makoto Naoi. N-methyl (r) salsolinol produces hydroxyl radicals: involvement to neurotoxicity. *Free Radical Biology and Medicine*, 19(1):67–75, 1995.

[30] Christian Amatore, Stéphane Arbault, Delphine Bruce, Pedro de Oliveira, Marie Erard, and Monique Vuillaume. Characterization of the electrochemical oxidation of peroxynitrite: relevance to oxidative stress bursts measured at the single cell level. *Chemistry–A European Journal*, 7(19):4171–4179, 2001.

[31] Yuhua Dong and Jianbin Zheng. Environmentally friendly synthesis of co-based zeolitic imidazolate framework and its application as h2o2 sensor. *Chemical Engineering Journal*, 392:123690, 2020.

[32] Jie Zhang, Yudong Sun, Xianchun Li, and Jiasheng Xu. Fabrication of nico2o4 nanobelt by a chemical co-precipitation method for non-enzymatic glucose electrochemical sensor application. *Journal of Alloys and Compounds*, 831:154796, 2020.

[33] Rafiq Ahmad, Min-Sang Ahn, and Yoon-Bong Hahn. Fabrication of a non-enzymatic glucose sensor field-effect transistor based on vertically-oriented zno nanorods modified with fe2o3. *Electrochemistry Communications*, 77:107–111, 2017.

[34] Jung-Chuan Chou, Yu-Hao Huang, Chih-Hsien Lai, Yu-Hsun Nien, Po-Yu Kuo, Tsu-Yang Lai, Tzu-Yu Su, and Zhi-Xuan Kang. Study of the glucose sensor based on potentiometric non-enzymatic nafion/czo thin film. *IEEE Sensors Journal*, 21(14):15926–15934, 2021.

[35] Rafiq Ahmad, Yoon-Bong Hahn, et al. Nonenzymatic flexible field-effect transistor based glucose sensor fabricated using nio quantum dots modified zno nanorods. *Journal of colloid and interface science*, 512:21–28, 2018.

[36] Yun Jung Heo, Hideaki Shibata, Teru Okitsu, Tetsuro Kawanishi, and Shoji Takeuchi. Long-term in vivo glucose monitoring using fluorescent hydrogel fibers. *Proceedings of the National Academy of Sciences*, 108(33):13399–13403, 2011.

[37] Soo-Youl Kim. Cancer energy metabolism: shutting power off cancer factory. *Biomolecules & Therapeutics*, 26(1):39, 2018.

[38] Arthur L Babson and Susan R Babson. Kinetic colorimetric measurement of serum lactate dehydrogenase activity. *Clinical chemistry*, 19(7):766–769, 1973.

[39] Ping Miao, Shile Sheng, Xiaoguang Sun, Jianjun Liu, and Gang Huang. Lactate dehydrogenase a in cancer: a promising target for diagnosis and therapy. *IUBMB life*, 65(11):904–910, 2013.

[40] Bin Hong and Youli Zu. Detecting circulating tumor cells: current challenges and new trends. *Theranostics*, 3(6):377, 2013.

[41] Sarvesh Varma, Anna Fendyur, Andrew Box, and Joel Voldman. Multiplexed cell-based sensors for assessing the impact of engineered systems and methods on cell health. *Analytical chemistry*, 89(8):4663–4670, 2017.

[42] Arshak Poghossian and Michael J Schöning. Label-free sensing of biomolecules with field-effect devices for clinical applications. *Electroanalysis*, 26(6):1197–1213, 2014.

[43] Jiehua Lin, Zhijing Wei, and Changming Mao. A label-free immunosensor based on modified mesoporous silica for simultaneous determination of tumor markers. *Biosensors and Bioelectronics*, 29(1):40–45, 2011.

[44] Julia D Wulfkuhle, Lance A Liotta, and Emanuel F Petricoin. Proteomic applications for the early detection of cancer. *Nature reviews cancer*, 3(4):267–275, 2003.

[45] Stephanie A Gajar and Michael W Geis. An ionic liquid-channel field-effect transistor. *Journal of the Electrochemical Society*, 139(10):2833–2840, 1992. doi: 10.1149/1.2068989.

[46] S. A. Gajar and M. W. Geis. An ionic liquid-channel field-effect transistor. *IEEE Transactions on Electron Devices*, 39(11):2649–2650, 1992. doi: 10.1109/16.163505.

[47] DY Kim and AJ Steckl. Liquid-state field-effect transistors using electrowetting. *Applied physics letters*, 90(4):043507, 2007. doi: 10.1063/1.2435508.

[48] J Matovic, N Adamovic, F Radovanovic, Z Jakšić, and U Schmid. Field effect transistor based on ions as charge carriers. *Sensors and Actuators B: Chemical*, 170:137–142, 2012. doi: 10.1016/j.snb.2011.03.011.

[49] Ranjan Kumar Maurya and Ajay Agarwal. Fluid-fet: an ionic controller for lab-on-a-chip. *IEEE Sensors Journal*, 15(11):6366–6373, 2015. doi: 10.1109/JSEN.2015.2456233.

[50] Rohit Karnik, Rong Fan, Min Yue, Deyu Li, Peidong Yang, and Arun Majumdar. Electrostatic control of ions and molecules in nanofluidic transistors. *Nano letters*, 5(5):943–948, 2005. doi: 10.1021/nl050493b.

[51] Shaurya Prakash and AT Conlisk. Field effect nanofluidics. *Lab on a Chip*, 16(20):3855–3865, 2016. doi: 10.1039/C6LC00688D.

[52] Marie Fuest, Caitlin Boone, Kaushik K Rangharajan, A Terrence Conlisk, and Shaurya Prakash. A three-state nanofluidic field effect switch. *Nano letters*, 15(4):2365–2371, 2015. doi: 10.1021/nl5046236.

[53] Sangwoo Shin, Beom Seok Kim, Jiwoon Song, Hwanseong Lee, and Hyung Hee Cho. A facile route for the fabrication of large-scale gate-all-around nanofluidic field-effect transistors with low leakage current. *Lab on a Chip*, 12(14):2568–2574, 2012. doi: 10.1039/C2LC40112F.

[54] Kee-Hyun Paik, Yang Liu, Vincent Tabard-Cossa, Matthew J Waugh, David E Huber, J Provine, Roger T Howe, Robert W Dutton, and Ronald W Davis. Control of dna capture by nanofluidic transistors. *ACS nano*, 6(8):6767–6775, 2012. doi: 10.1021/nn3014917.

[55] Qian Zhou, Youxiu Lin, Jian Shu, Kangyao Zhang, Zhenzhong Yu, and Dianping Tang. Reduced graphene oxide-functionalized feooh for signal-on photoelectrochemical sensing of prostate-specific antigen with bioresponsive controlled release system. *Biosensors and Bioelectronics*, 98:15–21, 2017.

[56] Qian Zhou, Youxiu Lin, Kangyao Zhang, Meijin Li, and Dianping Tang. Reduced graphene oxide/bifeo3 nanohybrids-based signal-on photoelectrochemical sensing system for prostate-specific antigen detection coupling with magnetic microfluidic device. *Biosensors and Bioelectronics*, 101:146–152, 2018.

[57] Shun Mao, Jingbo Chang, Haihui Pu, Ganhua Lu, Qiyuan He, Hua Zhang, and Junhong Chen. Two-dimensional nanomaterial-based field-effect transistors for chemical and biological sensing. *Chemical Society Reviews*, 46(22):6872–6904, 2017.

[58] Chengbin Liu, Xiaoyan Chen, Boyang Zong, and Shun Mao. Recent advances in sensitive and rapid mercury determination with graphene-based sensors. *Journal of Materials Chemistry A*, 7(12):6616–6630, 2019.

[59] Xiaoyan Chen, Ying Liu, Xian Fang, Zhuo Li, Haihui Pu, Jingbo Chang, Junhong Chen, and Shun Mao. Ultratrace antibiotic sensing using aptamer/graphene-based field-effect transistors. *Biosensors and Bioelectronics*, 126:664–671, 2019.

[60] Xiaoyan Chen, Haihui Pu, Zipeng Fu, Xiaoyu Sui, Jingbo Chang, Junhong Chen, and Shun Mao. Real-time and selective detection of nitrates in water using graphene-based field-effect transistor sensors. *Environmental Science: Nano*, 5(8):1990–1999, 2018.

[61] Edmilson Tinoco Vilela Jr, Rita de Cássia Silva Carvalho, Sakae Yotsumoto Neto, Rita de Cássia Silva Luz, and Flavio Santos Damos. Exploiting charge/ions compensating processes in pani/spani/reduced graphene oxide composite for development of a high sensitive h2o2 sensor. *Journal of Electroanalytical Chemistry*, 752:75–81, 2015.

[62] Tingting Zhang, Ruo Yuan, Yaqin Chai, Wenjuan Li, and Shujuan Ling. A novel nonenzymatic hydrogen peroxide sensor based on a polypyrrole nanowire-copper nanocomposite modified gold electrode. *Sensors*, 8(8):5141–5152, 2008.

[63] Jin Wook Park, Seon Joo Park, Oh Seok Kwon, Choonghyeon Lee, and Jyongsik Jang. Polypyrrole nanotube embedded reduced graphene oxide transducer for field-effect transistor-type h2o2 biosensor. *Analytical Chemistry*, 86(3):1822–1828, 2014.

[64] Jeong In Lee, Shin Hyo Cho, Su-Moon Park, Jin Kon Kim, Jai Kyeong Kim, Jae-Woong Yu, Young Chul Kim, and Thomas P Russell. Highly aligned ultrahigh density arrays of conducting polymer nanorods using block copolymer templates. *Nano letters*, 8(8):2315–2320, 2008.

[65] Radislav A Potyrailo. Polymeric sensor materials: toward an alliance of combinatorial and rational design tools? *Angewandte Chemie International Edition*, 45(5):702–723, 2006.

[66] Jian Shu, Zhenli Qiu, Shuzhen Lv, Kangyao Zhang, and Dianping Tang. Cu2+-doped sno2 nanograin/polypyrrole nanospheres with synergic enhanced properties for ultrasensitive room-temperature h2s gas sensing. *Analytical chemistry*, 89(20):11135–11142, 2017.

[67] Salma Bibi, Habib Ullah, Shah Masood Ahmad, Anwar-ul-Haq Ali Shah, Salma Bilal, Asif Ali Tahir, and Khurshid Ayub. Molecular and electronic structure elucidation of polypyrrole gas sensors. *The Journal of Physical Chemistry C*, 119(28):15994–16003, 2015.

[68] ST Navale, AT Mane, MA Chougule, RD Sakhare, SR Nalage, and VB Patil. Highly selective and sensitive room temperature no2 gas sensor based on polypyrrole thin films. *Synthetic Metals*, 189:94–99, 2014.

[69] Jian Shu, Zhenli Qiu, and Dianping Tang. Self-referenced smartphone imaging for visual screening of h2s using cu x o-polypyrrole conductive aerogel doped with graphene oxide framework. *Analytical chemistry*, 90(16):9691–9694, 2018.

[70] Aditee C Joshi, Ganesh B Markad, and Santosh K Haram. Rudimentary simple method for the decoration of graphene oxide with silver nanoparticles:

Their application for the amperometric detection of glucose in the human blood samples. *Electrochimica Acta*, 161:108–114, 2015.

[71] Jian Song, Lin Xu, Chunyang Zhou, Ruiqing Xing, Qilin Dai, Dali Liu, and Hongwei Song. Synthesis of graphene oxide based cuo nanoparticles composite electrode for highly enhanced nonenzymatic glucose detection. *ACS applied materials & interfaces*, 5(24):12928–12934, 2013.

[72] Reshmi Reghunath, KK Singh, et al. Recent advances in graphene based electrochemical glucose sensor. *Nano-Structures & Nano-Objects*, 26:100750, 2021.

[73] Ian V Lightcap, Thomas H Kosel, and Prashant V Kamat. Anchoring semiconductor and metal nanoparticles on a two-dimensional catalyst mat. storing and shuttling electrons with reduced graphene oxide. *Nano letters*, 10(2):577–583, 2010.

[74] Shijian Luo and CP Wong. Effect of uv/ozone treatment on surface tension and adhesion in electronic packaging. *IEEE Transactions on components and packaging technologies*, 24(1):43–49, 2001. doi: 10.1109/6144.910801.

[75] Gianmario Scotti, Petri Kanninen, Tanja Kallio, and Sami Franssila. Bulk-aluminum microfabrication for micro fuel cells. *Journal of Microelectromechanical Systems*, 23(2):372–379, 2014. doi: 10.1109/JMEMS.2013.2274592.

[76] Ann Witvrouw, Bert Du Bois, Piet De Moor, Agnes Verbist, Chris A Van Hoof, Hugo Bender, and Christiaan Baert. Comparison between wet hf etching and vapor hf etching for sacrificial oxide removal. In *Micromachining and Microfabrication Process Technology VI*, volume 4174, pages

130–141. International Society for Optics and Photonics, SPIE, 2000. doi: 10.1117/12.396423.

[77] Renate Förch, Holger Schönherr, and A Tobias A Jenkins. *Surface design: applications in bioscience and nanotechnology*. John Wiley & Sons, 2009.

[78] Reto B Schoch, Jongyoon Han, and Philippe Renaud. Transport phenomena in nanofluidics. *Reviews of modern physics*, 80(3):839–883, 2008. doi: 10.1103/RevModPhys.80.839.

[79] Mahmoud Khademi and Dominik PJ Barz. Structure of the electrical double layer revisited: Electrode capacitance in aqueous solutions. *Langmuir*, 36(16):4250–4260, 2020. doi: 10.1021/acs.langmuir.0c00024.

[80] D. J. Goss and R. H. Petrucci. *General Chemistry Principles & Modern Applications, Petrucci, Harwood, Herring, Madura:Study Guide*. Upper Saddle River, NJ, USA: Pearson, 2007.

[81] Kuan-Da Huang and Ruey-Jen Yang. Electrokinetic behaviour of overlapped electric double layers in nanofluidic channels. *Nanotechnology*, 18(11):115701, 2007. doi: 10.1088/0957-4484/18/11/115701.

[82] Youn-Jin Oh, Danny Bottenus, Cornelius F Ivory, and Sang M Han. Impact of leakage current and electrolysis on fet flow control and ph changes in nanofluidic channels. *Lab on a Chip*, 9(11):1609–1617, 2009.

[83] Adelmo Ortiz-Conde, FJ Garcıa Sánchez, Juin J Liou, Antonio Cerdeira, Magali Estrada, and Y Yue. A review of recent mosfet threshold voltage extraction methods. *Microelectronics reliability*, 42(4-5):583–596, 2002. doi: 10.1016/S0026-2714(02)00027-6.

[84] Adelmo Ortiz-Conde, Francisco J García-Sánchez, Juan Muci, Alberto Terán Barrios, Juin J Liou, and Ching-Sung Ho. Revisiting mosfet threshold voltage extraction methods. *Microelectronics Reliability*, 53(1):90–104, 2013. doi: 10.1016/j.microrel.2012.09.015.

[85] Peter Atkins, Peter William Atkins, and Julio de Paula. *Atkins' physical chemistry*. Oxford university press, 2014.

[86] Qicheng Chen, Jie Ma, Yingjin Zhang, Chunlei Wu, and Jinliang Xu. Effects of temperature and ionic concentration on nanodroplet electrocoalescence. *Langmuir*, 35(3):750–759, 2019. doi: 10.1021/acs.langmuir.8b03627.

[87] Puja Banerjee and Biman Bagchi. Ions' motion in water. *The Journal of Chemical Physics*, 150(19):190901, 2019. doi: 10.1063/1.5090765.

[88] Ryan Clark, Michael von Domaros, Alastair J. S. McIntosh, Alenka Luzar, Barbara Kirchner, and Tom Welton. Effect of an external electric field on the dynamics and intramolecular structures of ions in an ionic liquid. *The Journal of Chemical Physics*, 151(16):164503, 2019. doi: 10.1063/1.5129367.

[89] Seung-Hyun Lee, Hyomin Lee, Tianguang Jin, Sungmin Park, Byung Jun Yoon, Gun Yong Sung, Ki-Bum Kim, and Sung Jae Kim. Sub-10 nm transparent all-around-gated ambipolar ionic field effect transistor. *Nanoscale*, 7(3):936–946, 2015. doi: 10.1039/C4NR04089A.

[90] Monica Naorem, Rajan Singh, and Roy Paily. Ionic liquid channel field effect transistor fabricated using silicon dioxide trench. *IEEE Transactions on Electron Devices*, 68(9):4741–4747, 2021.

[91] F. S. de Souza, T. G. Costa, M. J. Feldhaus, B. Szpoganicz, and A. Spinelli. Nonenzymatic amperometric sensors for hydrogen peroxide

based on melanin-capped fe3+-, cu2+-, or ni2+-modified prussian blue nanoparticles. *IEEE Sensors Journal*, 15(9):4749–4757, 2015.

[92] Davide Vione, Valter Maurino, Claudio Minero, Daniele Borghesi, Mirco Lucchiari, and Ezio Pelizzetti. New processes in the environmental chemistry of nitrite. 2. the role of hydrogen peroxide. *Environmental Science & Technology*, 37(20):4635–4641, 2003.

[93] Xiaohong Shu, Ying Chen, Hongyan Yuan, Shangfeng Gao, and Dan Xiao. H2o2 sensor based on the room-temperature phosphorescence of nano tio2/sio2 composite. *Analytical Chemistry*, 79(10):3695–3702, 2007.

[94] Kenchaiah Sunil and Badiadka Narayana. Spectrophotometric determination of hydrogen peroxide in water and cream samples. *Bulletin of Environmental Contamination and Toxicology*, 81(4):422–426, 2008.

[95] Shiyi Xu, Bo Peng, and Xiaozu Han. A third-generation h2o2 biosensor based on horseradish peroxidase-labeled au nanoparticles self-assembled to hollow porous polymeric nanopheres. *Biosensors and Bioelectronics*, 22(8):1807–1810, 2007.

[96] Yujun Song, Weili Wei, and Xiaogang Qu. Colorimetric biosensing using smart materials. *Advanced Materials*, 23(37):4215–4236, 2011.

[97] Kun Wang, Qian Liu, Xiang-Yang Wu, Qing-Meng Guan, and He-Nan Li. Graphene enhanced electrochemiluminescence of cds nanocrystal for h2o2 sensing. *Talanta*, 82(1):372–376, 2010.

[98] Zhenzhong Yu, Shuzhen Lv, Rongrong Ren, Guoneng Cai, and Dianping Tang. Photoelectrochemical sensing of hydrogen peroxide at zero working

potential using a fluorine-doped tin oxide electrode modified with bivo 4 microrods. *Microchimica Acta*, 184(3):799–806, 2017.

[99] Yuping Lin, Xian Chen, Youxiu Lin, Qian Zhou, and Dianping Tang. Non-enzymatic sensing of hydrogen peroxide using a glassy carbon electrode modified with a nanocomposite made from carbon nanotubes and molybdenum disulfide. *Microchimica Acta*, 182(9):1803–1809, 2015.

[100] Seon Joo Park, Oh Seok Kwon, Sang Hun Lee, Hyun Seok Song, Tai Hyun Park, and Jyongsik Jang. Ultrasensitive flexible graphene based field-effect transistor (fet)-type bioelectronic nose. *Nano letters*, 12(10):5082–5090, 2012.

[101] Oh Seok Kwon, Seung Hwan Lee, Seon Joo Park, Ji Hyun An, Hyun Seok Song, Taejoon Kim, Joon Hak Oh, Joonwon Bae, Hyeonseok Yoon, Tai Hyun Park, et al. Large-scale graphene micropattern nano-biohybrids: high-performance transducers for fet-type flexible fluidic hiv immunoassays. *Advanced Materials*, 25(30):4177–4185, 2013.

[102] Keun-Young Shin, Jin-Yong Hong, and Jyongsik Jang. Micropatterning of graphene sheets by inkjet printing and its wideband dipole-antenna application. *Advanced materials*, 23(18):2113–2118, 2011.

[103] Zhengzong Sun, Zheng Yan, Jun Yao, Elvira Beitler, Yu Zhu, and James M Tour. Growth of graphene from solid carbon sources. *Nature*, 468(7323):549–552, 2010.

[104] Monica Naorem, Rajan Singh, and Roy Paily. Ionic liquid channel field effect transistor fabricated using silicon dioxide trench. *IEEE Transactions on Electron Devices*, July, 2021.

[105] Ning Cao and Yuan Zhang. Study of reduced graphene oxide preparation by hummers' method and related characterization. *Journal of Nanomaterials*, 2015, 2015.

[106] Yu Shang, Dong Zhang, Yanyun Liu, and Chao Guo. Preliminary comparison of different reduction methods of graphene oxide. *Bulletin of Materials Science*, 38(1):7–12, 2015.

[107] Rawoof A Naikoo and Radha Tomar. Fabrication of a novel zeolite-x/reduced graphene oxide/polypyrrole nanocomposite and its role in sensitive detection of co. *Materials Chemistry and Physics*, 211:225–233, 2018.

[108] Yun Liu, Huanhuan Wang, Jie Zhou, Linyi Bian, Enwei Zhu, Jiefeng Hai, Jian Tang, and Weihua Tang. Graphene/polypyrrole intercalating nanocomposites as supercapacitors electrode. *Electrochimica Acta*, 112:44–52, 2013.

[109] Jingfang Hu, Yueqi Li, Guowei Gao, and Shanhong Xia. A mediated bod biosensor based on immobilized b. subtilis on three-dimensional porous graphene-polypyrrole composite. *Sensors*, 17(11):2594, 2017.

[110] Su Pei Lim, Alagarsamy Pandikumar, Yee Seng Lim, Nay Ming Huang, and Hong Ngee Lim. In-situ electrochemically deposited polypyrrole nanoparticles incorporated reduced graphene oxide as an efficient counter electrode for platinum-free dye-sensitized solar cells. *Scientific reports*, 4(1):1–7, 2014.

[111] Oh Seok Kwon, Seon Joo Park, and Jyongsik Jang. A high-performance vegf aptamer functionalized polypyrrole nanotube biosensor. *Biomaterials*, 31(17):4740–4747, 2010.

[112] Chao Zheng, Xin Jin, Yutao Li, Junchi Mei, Yujie Sun, Mengmeng Xiao, Hong Zhang, Zhiyong Zhang, and Guo-Jun Zhang. Sensitive molybdenum

disulfide based field effect transistor sensor for real-time monitoring of hydrogen peroxide. *Scientific reports*, 9(1):1–9, 2019.

[113] Sang Hun Lee, Kyung Ho Kim, Sung Eun Seo, Mun il Kim, Seon Joo Park, and Oh Seok Kwon. Cytochrome c-decorated graphene field-effect transistor for highly sensitive hydrogen peroxide detection. *Journal of Industrial and Engineering Chemistry*, 83:29–34, 2020.

[114] Monica Naorem, Rajan Singh, and Roy Paily. Detection of hydrogen peroxide using rgo/ppy nanocomposites in silicon dioxide trench embedded field effect transistor. *IEEE Sensors Journal*, 21(20):22426–22433, 2021.

[115] Kala K Blakely and Kendra Weaver. Semaglutide is a new once-daily oral medication to treat type 2 diabetes. *Nursing for women's health*, 24(5):370—376, October 2020.

[116] Suping Ling, Karen Brown, Joanne K Miksza, Lynne M Howells, Amy Morrison, Eyad Issa, Thomas Yates, Kamlesh Khunti, Melanie J Davies, and Francesco Zaccardi. Risk of cancer incidence and mortality associated with diabetes: A systematic review with trend analysis of 203 cohorts. *Nutrition, Metabolism and Cardiovascular Diseases*, 31(1):14–22, 2021.

[117] Leland C Clark Jr and Champ Lyons. Electrode systems for continuous monitoring in cardiovascular surgery. *Annals of the New York Academy of sciences*, 102(1):29–45, 1962.

[118] Stuart J Updike and George P Hicks. The enzyme electrode. *Nature*, 214(5092):986–988, 1967.

[119] SJ Updike and GP Hicks. Reagentless substrate analysis with immobilized enzymes. *Science*, 158(3798):270–272, 1967.

[120] Sejin Park, Hankil Boo, and Taek Dong Chung. Electrochemical non-enzymatic glucose sensors. *Analytica chimica acta*, 556(1):46–57, 2006.

[121] Jing Li and Xiangqin Lin. Glucose biosensor based on immobilization of glucose oxidase in poly (o-aminophenol) film on polypyrrole-pt nanocomposite modified glassy carbon electrode. *Biosensors and Bioelectronics*, 22(12):2898–2905, 2007.

[122] Kathryn E Toghill and Richard G Compton. Electrochemical non-enzymatic glucose sensors: a perspective and an evaluation. *Int. J. Electrochem. Sci*, 5(9):1246–1301, 2010.

[123] Xiangheng Niu, Minbo Lan, Hongli Zhao, and Chen Chen. Highly sensitive and selective nonenzymatic detection of glucose using three-dimensional porous nickel nanostructures. *Analytical chemistry*, 85(7):3561–3569, 2013.

[124] Hua Zhu, Li Li, Wei Zhou, Zongping Shao, and Xianjian Chen. Advances in non-enzymatic glucose sensors based on metal oxides. *Journal of Materials Chemistry B*, 4(46):7333–7349, 2016.

[125] Xenofon Strakosas, John Selberg, Pattawong Pansodtee, Nebyu Yonas, Pattawut Manapongpun, Mircea Teodorescu, and Marco Rolandi. A non-enzymatic glucose sensor enabled by bioelectronic ph control. *Scientific reports*, 9(1):1–7, 2019.

[126] W Loeb. Sugar decomposition iii. electrolysis of dextrose. *Biochemische Zeitschrift Biochem*, (17):132–144, 1909.

[127] Rafiq Ahmad, Nirmalya Tripathy, Yoon-Bong Hahn, Ahmad Umar, Ahmed A Ibrahim, and SH Kim. A robust enzymeless glucose sensor based

on cuo nanoseed modified electrodes. *Dalton Transactions*, 44(28):12488–12492, 2015.

[128] Zhenyuan Ji, Yuqin Wang, Qiang Yu, Xiaoping Shen, Na Li, Hanyu Ma, Juan Yang, and Jiheng Wang. One-step thermal synthesis of nickel nanoparticles modified graphene sheets for enzymeless glucose detection. *Journal of colloid and interface science*, 506:678–684, 2017.

[129] Wen Wang, Liyan Kong, Jiaming Zhu, and Liang Tan. One-pot preparation of conductive composite containing boronic acid derivative for non-enzymatic glucose detection. *Journal of colloid and interface science*, 498:1–8, 2017.

[130] LY Chen, Takeshi Fujita, Y Ding, and MW Chen. A three-dimensional gold-decorated nanoporous copper core–shell composite for electrocatalysis and nonenzymatic biosensing. *Advanced Functional Materials*, 20(14):2279–2285, 2010.

[131] Guangfeng Wang, Xiuping He, Lingling Wang, Aixia Gu, Yan Huang, Bin Fang, Baoyou Geng, and Xiaojun Zhang. Non-enzymatic electrochemical sensing of glucose. *Microchimica Acta*, 180(3-4):161–186, 2013.

[132] Peng Si, Youju Huang, Taihong Wang, and Jianmin Ma. Nanomaterials for electrochemical non-enzymatic glucose biosensors. *RSC advances*, 3(11):3487–3502, 2013.

[133] Taejin Choi, Soo Hyeon Kim, Chang Wan Lee, Hangil Kim, Sang-Kyung Choi, Soo-Hyun Kim, Eunkyoung Kim, Jusang Park, and Hyungjun Kim. Synthesis of carbon nanotube–nickel nanocomposites using atomic layer de-

position for high-performance non-enzymatic glucose sensing. *Biosensors and Bioelectronics*, 63:325–330, 2015.

[134] E Mahmoudi, Law Yong Ng, Muneer M Ba-Abbad, and AW Mohammad. Novel nanohybrid polysulfone membrane embedded with silver nanoparticles on graphene oxide nanoplates. *Chemical Engineering Journal*, 277:1–10, 2015.

[135] Aline MZ de Medeiros, Latif U Khan, Gabriela H da Silva, Carlos A Ospina, Oswaldo L Alves, Vera Lúcia de Castro, and Diego Stéfani T Martinez. Graphene oxide-silver nanoparticle hybrid material: an integrated nanosafety study in zebrafish embryos. *Ecotoxicology and Environmental Safety*, 209:111776, 2021.

[136] Mónica Cobos, Iker De-La-Pinta, Guillermo Quindós, M Jesús Fernández, and M Dolores Fernández. Graphene oxide–silver nanoparticle nanohybrids: Synthesis, characterization, and antimicrobial properties. *Nanomaterials*, 10(2):376, 2020.

[137] Soumabha Bag, Ananya Baksi, Sree Harsha Nandam, Di Wang, Xinglong Ye, Jyotirmoy Ghosh, Thalappil Pradeep, and Horst Hahn. Nonenzymatic glucose sensing using ni60nb40 nanoglass. *ACS Nano*, 14(5):5543–5552, 2020. PMID: 32267141.

[138] Ashwini Kumar Mishra, Deepak Kumar Jarwal, Bratindranath Mukherjee, Amit Kumar, Smrity Ratan, and Satyabrata Jit. Cuo nanowire-based extended-gate field-effect-transistor (fet) for ph sensing and enzyme-free/receptor-free glucose sensing applications. *IEEE Sensors Journal*, 20(9):5039–5047, 2020.

[139] Qi Mao, Weixuan Jing, Fan Zhou, Shu Liu, Weizhuo Gao, Zhengying Wei, and Zhuangde Jiang. Depositing reduced graphene oxide on zno nanorods to improve the performance of enzymatic glucose sensors. *Materials Science in Semiconductor Processing*, 121:105391, 2021.

[140] Nghia Duc Nguyen, Tuan Van Nguyen, Anh Duc Chu, Hoang Vinh Tran, Luyen Thi Tran, and Chinh Dang Huynh. A label-free colorimetric sensor based on silver nanoparticles directed to hydrogen peroxide and glucose. *Arabian Journal of Chemistry*, 11(7):1134–1143, 2018.

[141] Ali A. Ensafi, N. Zandi-Atashbar, B. Rezaei, M. Ghiaci, M. Esmaeili Chermahini, and P. Moshiri. Non-enzymatic glucose electrochemical sensor based on silver nanoparticle decorated organic functionalized multiwall carbon nanotubes. *RSC Adv.*, 6:60926–60932, 2016.

[142] Balamurali Kannan, Sana Jahanshahi-Anbuhi, Robert H Pelton, Yingfu Li, Carlos D M Filipe, and John D Brennan. Printed paper sensors for serum lactate dehydrogenase using pullulan-based inks to immobilize reagents. *Analytical chemistry*, 87(18):9288–9293, 2015.

[143] Federica Catania, Elena Marras, Mauro Giorcelli, Pravin Jagdale, Luca Lavagna, Alberto Tagliaferro, and Mattia Bartoli. A review on recent advancements of graphene and graphene-related materials in biological applications. *Applied Sciences*, 11(2):614, 2021.

[144] M Jannathul Firdhouse and P Lalitha. Biosynthesis of silver nanoparticles and its applications. *Journal of Nanotechnology*, 2015, 2015.

[145] Zhi Zhang, Wenfei Shen, Jing Xue, Yuanmeng Liu, Yanwei Liu, Peipei Yan, Jixian Liu, and Jianguo Tang. Recent advances in synthetic methods and

applications of silver nanostructures. *Nanoscale Research Letters*, 13(1):1–18, 2018.

[146] Abdolhassan Talaiezadeh, Ali Shahriari, Mohammad Reza Tabandeh, Payam Fathizadeh, and Siavash Mansouri. Kinetic characterization of lactate dehydrogenase in normal and malignant human breast tissues. *Cancer cell international*, 15(1):1–9, 2015.

List of Publications

Journal Publications

1. **M. Naorem**, R. Singh and R. Paily, "Ionic Liquid Channel Field Effect Transistor Fabricated Using Silicon Dioxide Trench", in *IEEE Transactions on Electron Devices,* vol. 68, no. 9, pp. 4741-4747, Sept. 2021, doi: 10.1109/TED.2021.3096783.

2. **M. Naorem**, R. Singh and R. Paily, "Detection of Hydrogen Peroxide Using rGO/PPy Nanocomposites in Silicon Dioxide Trench Embedded Field Effect Transistor," in *IEEE Sensors Journal*, vol. 21, no. 20, pp. 22426-22433, 15 Oct.15, 2021, doi: 10.1109/JSEN.2021.3106248.

3. **M. Naorem** and R. Paily, "Non-enzymatic glucose detection using GO/Ag NPs in Silicon Dioxide Trench Embedded Field Effect Transistor," in *IEEE Sensors Journal.*

4. S. Ghosh, **M. Naorem**, R. Singh and R. Paily, "Non-enzymatic Urea Sensing with Cys-GO using Device with Silicon Dioxide Trench," in *IEEE Sensors Journal.*

5. **M. Naorem** and R. Paily,"Fabrication and characterization of SiO_2 trench with different channel lengths " (Under Preparation).

6. **M. Naorem**, P. Sen, R. Singh, R. Paily and S.S. Ghosh,"Lactate functionalised GO/Ag NPs for LDH detection and temperature dependence analysis" (Under Preparation).

7. **M. Naorem**, P. Sen, R. Paily and S.S. Ghosh, "Lactate functionalised GO/Ag NPs FET for label free cancer cell's secreted LDH sensing" (Under Preparation).

Conferences

1. **M. Naorem**, R. Singh and R. Paily,"Fabrication of Silicon dioxide trench using photolithography technique," in *6th International Conference on Advanced Nanomaterial and Nanotechnology (ICANN-2019),*, IIT Guwahati, India, 2019. (Poster)

Patents

1. **M. Naorem**, P. Sen, R. Singh, R. Paily and S.S. Ghosh, "Lactate functionalised GO/Ag NPs for LDH detection and temperature dependence analysis", 202231008246, 2022

2. R. Singh, M. Saha, **M. Naorem**, R. Singh, R. Paily and S.S. Ghosh, "A chemiresistor biosensor device for detection of GSH", 202231020350,, 2022

3. **M. Naorem**, P. Sen, R. Paily and S.S. Ghosh, "Lactate functionalised GO/Ag NPs FET for label free cancer cell's secreted LDH sensing" (Patent under Preparation).